

Access to this work was provided by the University of Maryland, Baltimore County (UMBC) ScholarWorks@UMBC digital repository on the Maryland Shared Open Access (MD-SOAR) platform.

Please provide feedback

Please support the ScholarWorks@UMBC repository by emailing scholarworks-group@umbc.edu and telling us what having access to this work means to you and why it's important to you. Thank you.

SIGNATURES OF YOUNG STAR FORMATION ACTIVITY WITHIN TWO PARSECS OF Sgr A*

F. YUSEF-ZADEH¹, M. WARDLE², M. SEWILLO³, D. A. ROBERTS¹, I. SMITH², R. ARENDT⁴, W. COTTON⁵, J. LACY⁶, S. MARTIN⁷,
M. W. POUND⁸, M. RICKERT¹, AND M. ROYSTER¹¹ Department of Physics and Astronomy and CIERA, Northwestern University, Evanston, IL 60208, USA² Department of Physics and Astronomy, and Research Center for Astronomy, Astrophysics & Astrophotonics, Macquarie University, Sydney NSW 2109, Australia³ Space Science Institute, 4750 Walnut St. Suite 205, Boulder, CO 80301, USA⁴ CRESST/UMBC/NASA GSFC, Code 665, Greenbelt, MD 20771, USA⁵ National Radio Astronomy Observatory, Charlottesville, VA 22903, USA⁶ Department of Astronomy, University of Texas, Austin, TX 78712, USA⁷ Institut de Radio Astronomie Millimétrique, 300 rue de la Piscine, Dom. Univ., F-38406 St Martin d'Hères, France⁸ Department of Astronomy, University of Maryland, College Park, MD 20742, USA

Received 2015 January 25; accepted 2015 May 15; published 2015 July 23

ABSTRACT

We present radio and infrared observations indicating ongoing star formation activity inside the $\sim 2\text{--}5$ pc circumnuclear ring at the Galactic center. Collectively these measurements suggest a continued disk-based mode of ongoing star formation has taken place near Sgr A* over the last few million years. First, Very Large Array observations with spatial resolution $2''.17 \times 0''.81$ reveal 13 water masers, several of which have multiple velocity components. The presence of interstellar water masers suggests gas densities that are sufficient for self-gravity to overcome the tidal shear of the $4 \times 10^6 M_\odot$ black hole. Second, spectral energy distribution modeling of stellar sources indicates massive young stellar object (YSO) candidates interior to the molecular ring, supporting in situ star formation near Sgr A* and appear to show a distribution similar to that of the counter-rotating disks of ~ 100 OB stars orbiting Sgr A*. Some YSO candidates (e.g., IRS 5) have bow shock structures, suggesting that they have gaseous disks that are phototoevaporated and photoionized by the strong radiation field. Third, we detect clumps of SiO (2-1) and (5-4) line emission in the ring based on Combined Array for Research in Millimeter-wave Astronomy and Sub-Millimeter Array observations. The FWHM and luminosity of the SiO emission is consistent with shocked protostellar outflows. Fourth, two linear ionized features with an extent of ~ 0.8 pc show blue and redshifted velocities between $+50$ and -40 km s⁻¹, suggesting protostellar jet driven outflows with mass-loss rates of $\sim 5 \times 10^{-5} M_\odot \text{ yr}^{-1}$. Finally, we present the imprint of radio dark clouds at 44 GHz, representing a reservoir of molecular gas that feeds star formation activity close to Sgr A*.

Key words: Galaxy: center – ISM: clouds – ISM: general – stars: black hole – stars: formation – stars: protostars

1. INTRODUCTION

A critical question regarding star formation activity near supermassive black holes (SMBHs) is whether tidal shear in the vicinity of SMBHs is able to completely suppress star formation or whether it enables a disk-based mode of star formation, entirely distinct from the standard cloud-based mode observed in the Galactic disk. The molecular ring orbiting the $4 \times 10^6 M_\odot$ black hole Sgr A* in the inner few parsecs of the Galactic center is an excellent testing ground to examine how star formation proceeds in the extreme tidally sheared environment of an SMBH.

A fragile and kinematically disturbed circumnuclear molecular ring (CMR), also known as the circumnuclear molecular disk (CND), orbits Sgr A* with a velocity of 110 km s⁻¹ and is about 2–7 pc in extent (Christopher et al. 2005; Etzaluze et al. 2006; Goicoechea et al. 2013; Jackson et al. 1993; Montero-Castaño et al. 2009). The Roche number density required for self-gravity to overcome tidal shear is $n \sim 2 \times 10^8 \text{ cm}^{-3}$ at 1 pc from Sgr A* and is substantially higher at subparsec distances ($n \propto r^{-3}$). HCN (1-0) observations (Christopher et al. 2005) infer that the clumps in the CMR have densities greater than the critical Roche density and that star formation can take place in the molecular ring. However, the implied mass of the CMR exceeds $10^5 M_\odot$ and is inconsistent with far-infrared (FIR) dust emission and the lack of dynamical effects attributed to gravitational potential of the ring (Genzel et al. 2010). Indeed, recent analysis of molecular line data

suggests that the density in the ring has been overestimated by one to two orders of magnitude (Requena-Torres et al. 2012; Mills et al. 2013; Smith & Wardle 2014), implying that the gas is generally tidally unstable against self-gravity. Nevertheless, star formation has taken place in this region in the last few million years, as evidenced by a population of more than 100 OB stars distributed in two disks orbiting clockwise and counterclockwise within $10''$ (0.4 pc) of Sgr A* (Tanner et al. 2005; Beloborodov et al. 2006; Paumard et al. 2006; Lu et al. 2009). Theoretical models have been proposed to explain star formation in this environment (Nayakshin et al. 2007; Bonnell & Rice 2008; Wardle & Yusef-Zadeh 2008, 2012, 2014; Mapelli et al. 2012, 2013; Jalali et al. 2014).

Motivated by the discovery of young stars near Sgr A*, we have previously searched for signs of ongoing star formation on different scales. On subparsec scales, ALMA observations of the interior of the molecular ring detected SiO (5-4) emission from 11 clumps (Yusef-Zadeh et al. 2013). The full line widths as a function of the luminosity of SiO (5-4) line emission are similar to those of low- and high-mass protostellar systems in the Galactic disk (Gibb et al. 2004, 2007). This led to the suggestion that SiO emission clumps trace protostellar outflows from young stellar objects (YSOs). This interpretation was supported by spectral energy distribution (SED) modeling of stellar sources using *Spitzer Space Telescope* (*Spitzer*) and the 2MASS data, which identified two YSO candidates near SiO clumps (Yusef-Zadeh et al. 2013).

Table 1
The Coordinates and Flux Density of Water Masers in the CMR

Galactic Coordinates	Name	R.A. 1 σ	Decl. 1 σ	Peak Velocity ^a	Peak Flux 1 σ	Cross-reference
G359.957-0.050	1A	17 45 42.735 ± 0.003	-28 59 57.390 ± 0.078	47.29 km s ⁻¹	113.2 mJy ± 2.8	Sjouwerman et al. (2002)
	1B	5-4.04	100.6	...
	1C	58.26	55.5	...
	1D	63.33	44.9	...
G359.954-0.041	2A	17 45 40.171 ± 0.001	-28 59 47.818 ± 0.032	5-4.04	278.1 ± 2.8	...
	2B	56.57	62.9	...
G359.956-0.035	3	17 45 39.309 ± 0.010	-28 59 30.127 ± 0.163	5.07	88.0 ± 2.8	...
	4	17 45 38.623 ± 0.003	-29 00 5-4.226 ± 0.098	-81.91	91.0 ± 2.8	Li et al. (2010)
G359.932-0.045	5A	17 45 38.026 ± 0.001	-29 01 02.634 ± 0.037	2.53	244.2 ± 2.8	...
	5B	6.75	22.6	...
	5C	10.13	27.9	...
G359.925-0.053	6A	17 45 38.954 ± 0.002	-29 01 39.466 ± 0.086	-8.44	30.4 ± 2.8	...
	6B	-3.37	19.8	...
	6C	0.84	39.9	...
	6D	5.06	118.8	...
G359.934-0.050	7A	17 45 40.148 ± 0.006	-29 00 55.388 ± 0.146	22.79	74.5 ± 2.8	...
	7B	27.02	30.2	...
G359.939-0.052	8A	17 45 40.656 ± 0.006	-29 00 55.679 ± 0.146	38.84	100.2 ± 2.8	...
	8B	67.55	130.7	...
G359.938-0.064	9	17 45 43.310 ± 0.001	-29 01 18.880 ± 0.048	-40.53	185.7 ± 2.8	...
	10	17 45 44.747 ± 0.003	-29 01 09.019 ± 0.085	-43.06	143.1 ± 2.8	...
G359.954-0.053	11A	17 45 43.022 ± 0.003	-29 00 11.890 ± 0.131	-70.93	43.4 ± 2.8	...
	11B	-63.33	81.6	...
G359.954-0.054	12	17 45 43.109 ± 0.003	-29 00 13.050 ± 0.096	32.93	104.4 ± 2.8	...
	13A	17 45 44.326 ± 0.001	-28 59 13.310 ± 0.031	78.53	289.2 ± 2.8	Sjouwerman et al. (2002)
G359.957-0.050	13B	80.22	319.6	...
	13C	81.90	160.3	...
	13D	87.81	268.0	...
	13E	91.19	99.8	...

Note.

^a The uncertainty is 0.84 km s⁻¹, corresponding to the channel width.

In a second study, we detected seven collisionally excited $7_0 - 6_1A^+$ methanol masers (44.0694 GHz) and water masers (22.23419 GHz) within 2 pc of Sgr A* with the Green Bank Telescope (GBT; Yusef-Zadeh et al. 2008, hereafter YBWR08). The association of CH₃OH and H₂O masers with molecular clumps in the ring suggested that hot cores and YSO outflows may be present. However, interstellar and stellar water masers cannot be distinguished in low spatial resolution data, so the suggestion that water masers trace ongoing star formation is tentative.

Here we present five different studies supporting star formation activity within the inner 2 pc of Sgr A*. After describing the multi-wavelength observations in Section 2, we first focus in Section 3.1 on high-resolution observations of interstellar 22 GHz water maser line emission. Second, we

concentrate in Section 3.2 on SED fitting of the YSO models to infrared excess stellar sources. We discuss individual YSO candidates and note their similar distribution to the counter-rotating stellar disks orbiting Sgr A*. Third, we present in Section 3.3 SiO (2-1) and SiO (5-4) line emission from the inner 3' of the CMR. Fourth, we present kinematics of an ionized linear feature in Section 3.4, which we interpret as a protostellar jet from a YSO. Finally, in Section 3.5, we argue that as molecular clouds are bathed in the intense radiation field of the Galactic center, they manifest regions of suppressed radio continuum emission (Yusef-Zadeh 2012). Identification of such “radio dark clouds” implies that there is a supply of dense gas feeding star formation activity near Sgr A*.

2. OBSERVATIONS AND DATA REDUCTIONS

In the following sections, we briefly describe the data used for our analysis. The water maser data are presented here for the first time; the rest of the data have already been either completely or partly published in the past (see references below).

2.1. Present Data

2.1.1. H_2O Line at 22 GHz

Water maser observations were carried out with the Karl G. Jansky Very Large Array (VLA) in its B-configuration on 2012 February 2. The observations used the new correlator to sample 256 channels at 62.5 kHz (0.84 km s^{-1}). During the hour-long observations, we alternated between two pointing positions at α, δ (J2000) = $17^{\text{h}}45^{\text{m}}43^{\text{s}}, -29^{\circ}00'00''$ and $17^{\text{h}}45^{\text{m}}39^{\text{s}}, -29^{\circ}01'00''$. 3C286 was used as a primary flux calibrator and NRAO530 as the complex gain and bandpass calibrator. The data were calibrated in the usual manner using AIPS. Data for both pointings were phase self-calibrated using Sgr A* as a point-source model. Continuum subtraction in the visibility plane was carried out using the UVLSF task of AIPS before mosaic images were constructed with spatial and spectral resolutions of $2''.17 \times 0''.81$ (PA = $-10^{\circ}9$) and 0.9 km s^{-1} , respectively. The rms noise in each channel map is about $2.8 \text{ mJy beam}^{-1}$.

2.2. Published Data

2.2.1. SiO (2-1) and (5-4) Lines

The SiO (2-1) line data were taken with the Combined Array for Research in Millimeter-wave Astronomy (CARMA)⁹ during the 2009 and 2010 observing seasons in the D and C array configurations. The array consisted of six 10.4 m antennas and nine 6.1 m antennas and the maps were made on a 127 point hexagonal mosaic covering 7.1 arcmin, Nyquist-sampling the 10.4 m antenna primary beam. The spatial resolution and spectral resolutions of the final maps are $6''.8 \times 3''.7$ (PA = $1^{\circ}2$) and 6.74 km s^{-1} , respectively, covering a total LSR velocity range from -180 to 180 km s^{-1} .

We also used the SiO (5-4) line data taken with the Sub-Millimeter Array (SMA). Details of these observations are very similar to the data presented in Martin et al. (2012) except that an additional track of data was added using the SMA in its compact configuration. After applying uniform weighting to UV data, the CMR was mapped in its entirety in the SiO (5-4) line with a spatial and spectral resolution of $3''.6 \times 2''.4$ and 2 km s^{-1} respectively, covering a total velocity range between -140 and 140 km s^{-1} .

2.2.2. [Ne II] Line and $12.8 \mu\text{m}$ Continuum

Details of the [Ne II] line observations are given in Yusef-Zadeh et al. (2010) and Irons et al. (2012). Briefly, Sgr A West was observed in the [Ne II] ($12.8 \mu\text{m}$) line with the high-resolution mid-infrared spectrograph TEXES on the NASA IRTF on 2009 June 3 and 2010 May 30 (UT). TEXES (Lacy et al. 2002) used high-resolution, cross-dispersed, with velocity resolution $\sim 4 \text{ km s}^{-1}$ and spatial resolution $\sim 1''.2$ along a

$1''.4 \times 7''.5$ slit. The data were first processed with the standard TEXES pipeline reduction program. The absolute astrometry of the $12.8 \mu\text{m}$ data is a few arcseconds. We obtained coordinates for the [Ne II] maps by aligning them with the radio continuum maps with positional errors of $\sim 0''.35$ (1 pixel). This is because the position of the strong radio source Sgr A* is accurately known in radio continuum images taken with VLA.

2.2.3. Mid-IR Data

We used the published data obtained with the Very Large Telescope (VLT) at wavelengths ranging between 1.6 and $19.5 \mu\text{m}$ (Viehmman et al. 2006). This data set comprised of high-resolution and high-sensitivity observations of stellar sources near Sgr A*. The data points for SED fitting (see Section 3.2) are taken from Table 1 of Viehmman et al. (2006).¹⁰

3. RESULTS AND DISCUSSION

3.1. Water Masers

We detect 13 water masers concentrated toward the inner edge of the molecular ring. Figure 1 shows the distribution of water masers (crosses) superimposed on an image of the velocity-integrated HCN (1-0) line (Christopher et al. 2005); The insets show their spectra. Entries in Columns 1–7 in Table 1 give Galactic coordinates, source name, celestial coordinates, the peak flux, the peak velocity, and cross references for all detected masers. A large-scale water maser survey toward the Galactic center using ATCA did not detect any of the sources reported here because of their lower sensitivity with rms noise $\sigma \sim 0.1 \text{ Jy}$ (Caswell et al. 2011). Table 1 lists multiple velocity components in several sources with peak velocities ranging between ~ -91 and 67 km s^{-1} . The peak fluxes range between 22.6 and $319.6 \text{ mJy beam}^{-1}$, corresponding to brightness temperatures ranging between ~ 0.6 and 7.9 K . These sources are spatially unresolved, and thus these brightness temperatures are lower limits. We regard these sources as masers because of their narrow line widths of $\sim 1 \text{ km s}^{-1}$.

The HCN (1-0) observations resolved 26 cores with a typical diameter of $\sim 7''$ (0.25 pc). Three collisionally excited methanol masers coincide with 3 of 26 HCN clumps F, G, and V, drawn as circles centered on masers in Figure 1 (YBWR08). The region to the NE of the molecular ring in Figure 1 shows three water masers (1, 11, and 12) and two methanol masers coincident with the clumps labeled F and G, in the HCN (1-0) line map (Christopher et al. 2005; YBWR08). The methanol spectrum in the vicinity of clump F has three narrow velocity peaks between 52 and 55 km s^{-1} and a broad redshifted wing extending up to 100 km s^{-1} (YBWR08). This region is inferred to be a star-forming site because of the collisionally excited methanol maser at 44 GHz and the redshifted broad wing in the HCN (1-0) line with a peak velocity of $\sim 60 \text{ km s}^{-1}$ (YBWR08). The velocity correlation of 22 GHz masers and molecular line emission, SiO (5-4) and HCN (1-0), will be discussed in Section 3.3.3.

It is possible that interstellar water lines are contaminated by water lines from evolved OH/IR stars in this highly confused

⁹ Ongoing CARMA development and operations are supported by the National Science Foundation and the CARMA partner universities.

¹⁰ The relative coordinates of stars, which are misprinted in their Table 1, are with respect to IRS 7 at α, δ (J2000) $17^{\text{h}}45^{\text{m}}40^{\text{s}}.040, -29^{\circ}00'22''.56$ (A. Exkart, private communication).

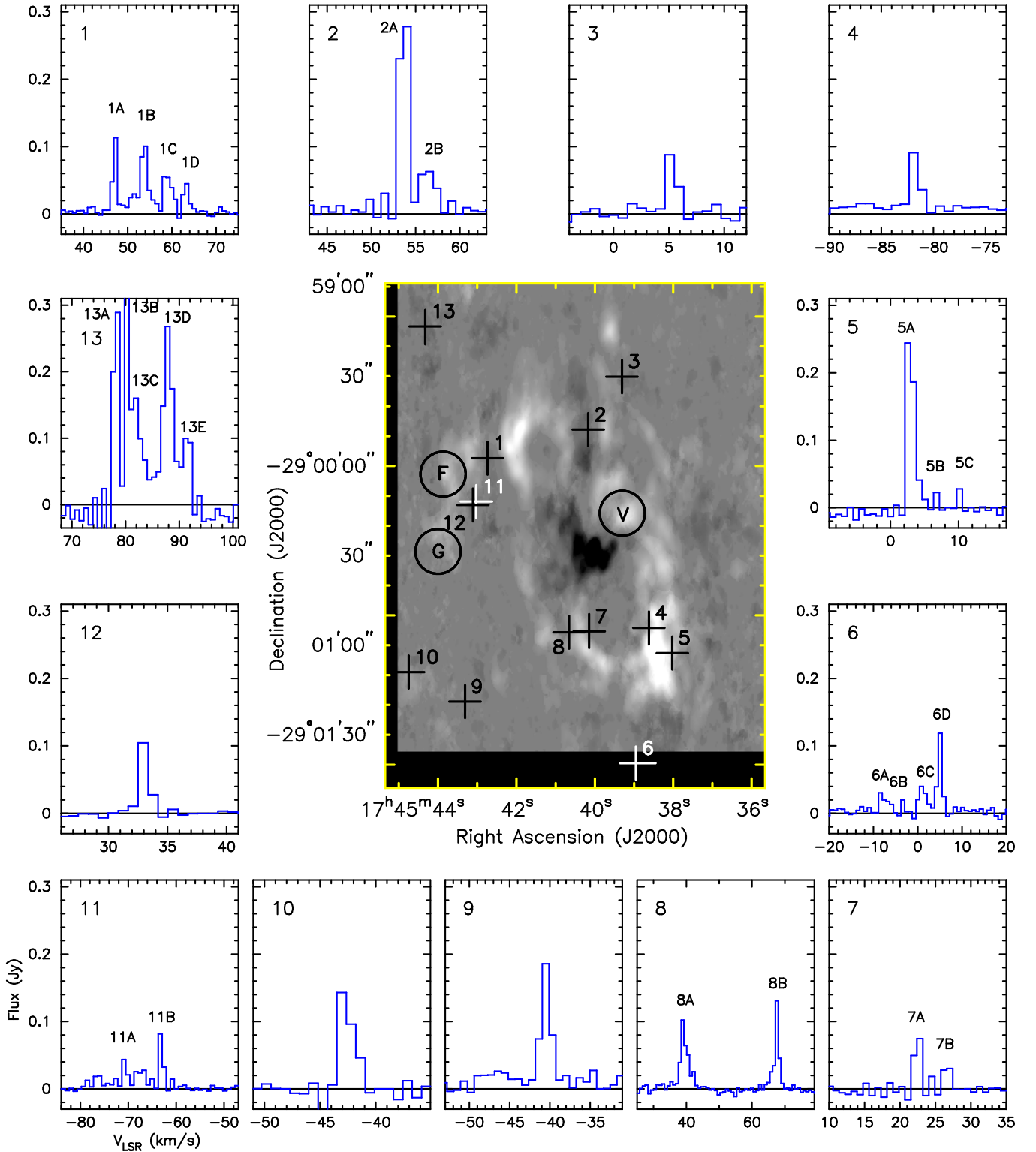


Figure 1. Positions of water masers (this work) and collisionally excited methanol masers (YBWR08) are drawn as crosses and circles, respectively, on a HCN(1-0) map (Christopher et al. 2005). The sizes of the circles correspond to the spatial resolution of Green Bank Telescope (GBT) observations (FWHM $\sim 15''$; Yusef-Zadeh et al. 2008). The surrounding plots show the spectra of 13 water masers.

region of the Galaxy. To exclude this possibility, we compared the position of new water masers listed in Table 1 with those of OH/IR stars and SiO masers associated with evolved stars. With the exception of sources 1 and 13 (Lindqvist et al. 1992; Levine et al. 1995; Sjouwerman & van Langevelde 1996; Sjouwerman et al. 2002; Li et al. 2010), we did not find

evolved stellar counterparts with similar velocities and positions to those of detected water masers in Table 1. Water maser 1 coincides with an OH/IR star 359.956-0.050 2a (Table 2 of Sjouwerman et al. 2002), although it is not clear why this water maser has four velocity components 47, 54, 58, and 63 km s^{-1} (Table 1) when the velocity profile of the OH/IR star

has only two velocity components (Sjouwerman et al. 2002). These velocity components match up with those of collisionally excited methanol line emission (YBWR08). Similarly, maser 13 also shows five velocity peaks, 78.53, 80.22, 81.90, 87.81, 91. and 19 km s⁻¹ (Table 1), and is spatially coincident with the OH/IR star 359.970-0.049, with two velocity peaks of 37.5 and 94.5 km s⁻¹ (Sjouwerman et al. 2002). The spectrum of maser 8 appears to be similar to that of an OH/IR star.

Among other water masers, we note that water maser 11 shows two forbidden velocities -63 and -71 km s⁻¹ assuming orbits aligned with the Galactic rotation. An SiO maser source, denoted SiO-18 in Table 2 of Li et al. (2010) is located within a few arcseconds of water maser source 4. However, the peak emission from SiO-18 is at 39.6 km s⁻¹ whereas water maser source 4 has a peak velocity of -82 km s⁻¹, suggesting that they are not associated with each other. We note that water maser 6 has more than three peaks like water maser 1 and 13. OH/IR stars are identified by two peaks symmetrically centered around the velocity of the central star, so water masers with more than two velocity components are unlikely to be associated with individual OH/IR stars. It is possible that these sources with multiple velocity components are interstellar water masers but are contaminated by OH/IR stars. Water maser 8 has two components that are much more widely separated in velocity than other water masers' components. In summary, we have detected a total of five water masers with three or more (1, 5, 6, 11, and 13) velocity components, five water masers with a single velocity component (3, 4, 9, 10, and 12) and three water masers with two velocity components (3, 7, and 8). Water masers with double velocity components are probably associated with OH/IR stars whereas the remaining sources are likely to be associated with interstellar masers.

3.2. YSO Candidates and Star Formation Rate

The detection of water and collisionally excited methanol masers motivated us to search for YSOs within the inner parsec of Sgr A*. This region is populated by about 60 dusty and red sources that could be OH/IR stars and/or YSO candidates, both of which have strong infrared excess emission (Viehmann et al. 2005, 2006). OH/IR stars represent evolved AGB stars at the end of their lives (Habing 1996) whereas YSOs are characterized by dusty envelopes and disks that absorb the radiation from the central protostar (e.g., Whitney et al. 2003). Near- and mid-IR photometric observations with VLT have identified a total of 64 sources in the central parsec at wavelengths ranging between 1.6 μ m (H band) and 19.5 μ m (Q band), respectively (Viehmann et al. 2006). Four types of sources were classified based on their SEDs (Viehmann et al. 2006; Preger et al. 2008). Type I consists of luminous IR sources that are embedded in the N arm ionized streamers. These sources (e.g., IRS 1, IRS 2L, IRS 10W, and IRS 21), showing bow-shock structures with featureless SEDs that peak in the mid-IR wavelengths, are generally thought to be interacting with the mini-spiral (Tanner et al. 2005). Type II consists of low-luminosity sources that have similar bow shock morphology to those of Type I sources, but are offset from the mini-spiral streamers. Type III sources are cool stars with SEDs that peak in the near-IR wavelengths. Last, Type IV sources are hot stars (e.g., IRS 16NE, IRS 16NW, AF, and AHH) with SEDs that peak at shorter wavelengths. There are also a number of sources that could not be classified among these four types based on their SEDs (Viehmann et al. 2006).

We carried out YSO SED fitting of dusty sources of all types listed in Table 1 of Viehmann et al. (2006) to provide additional constraints on the nature of these sources. We used the same technique that identified a population of YSO candidates toward the inner few 100 pc of the Galaxy (Yusef-Zadeh et al. 2009, but see Koepferl et al. 2015). To obtain reliable fits, we only selected sources with at least four flux measurements (52 out of 64 sources). The Viehmann et al. (2006) observations used nine VLT/VISIR bands in the wavelength range from 1.6 to 19.5 μ m, with an angular resolution (FWHM) of 0''.3-0''.6. We considered using the catalog of near-IR sources (Schödel et al. 2010) for additional data points for those sources that had limited data in Viehmann et al. (2006). However, the lack of proper motion data and confusing sources prevented us from using the new catalog at H, J, and L' bands (Schödel et al. 2010). The availability of data from a single instrument that provides a broad wavelength range and high angular resolution minimizes source confusion and systematic effects.

We compare the sources' SEDs to the Robitaille et al. (2006) large grid of pre-computed YSO model SEDs using the linear regression SED fitting tool developed by Robitaille et al. (2007). We consider models with interstellar extinction (A_V) between 2.5 and 30 mag, and distance between 7.65 and 9.35 kpc (i.e., the distance to the Galactic center of $8.5 \text{ kpc} \pm 10\%$). We identify well-fit models as those with a normalized χ^2 per data point (χ^2/pt) less than 3. As a result, only 19 out of 52 sources are well-fit by YSO models. A good YSO model fit indicates that the source's SED is consistent with the YSO model SED, but does not provide a definite classification.

We estimate physical parameters of these sources by averaging parameters of all YSO models that fit the source's SED with χ^2/pt in a range between the χ^2/pt for the best-fitting model (χ^2_{\min}/pt) and ($\chi^2_{\min}/pt + 2$). The visual examination of the fits showed that the YSO model fits with χ^2/pt within this arbitrary range provide acceptable fits to the SEDs (see Figure 2). The fitting results are presented in Table 2. In Column 1, we provide the Viehmann et al. (2006) ID numbers (V06 ID). Columns 2 and 3 list the χ^2/pt for the best-fit model (χ^2_{\min}/pt) and the number of acceptable fits (n_{fits}), respectively. In Columns 4-15, we provide the estimates of the physical parameters for the best-fit model, as well as the average physical parameters calculated based on all the acceptable fits (see above). The physical parameters include the interstellar extinction (A_V), stellar luminosity (L_*), temperature (T_*), and mass (M_*), as well as the envelope mass (M_{env}), and disk mass (M_{disk}). The best and average evolutionary stages (Columns 16-17) are based on sources' physical parameters as defined by Robitaille et al. (2006). Column 18 gives the number of data points used for the SED fitting.

Stage I objects are young protostars embedded in an opaque infalling envelope. In Stage II are objects the envelope has mostly dispersed, and the central star is surrounded by an opaque disk. In Stage III the disk is optically thin. The SEDs of sources that are well-fit with YSO models are shown in Figure 2. In each plot, the best-fit model and all acceptable models are shown in black and gray, respectively. The dashed line is the central stellar atmosphere corresponding to the best-fit model, extincted by the fitted foreground extinction. To place additional constraints on best-fit models, we explored the possibility of using *Herschel* data at long wavelengths.

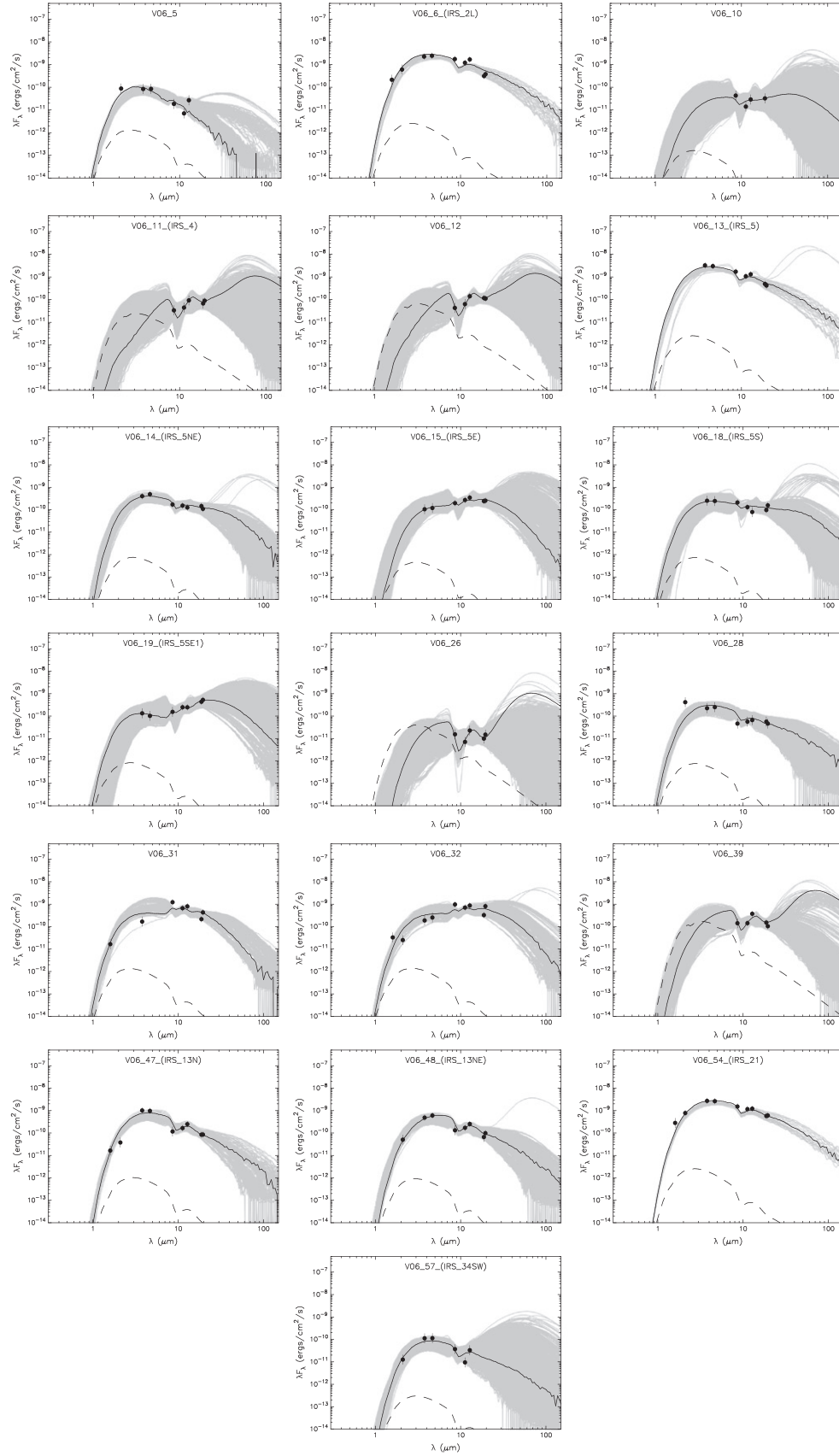


Figure 2. SEDs and YSO model fits for 19 YSO candidates well fit with YSO models. The sources are located in the central YSO cluster near Sgr A*. Filled circles are flux values from the Viehmann et al. (2006) VLT/VISIR observations (1.6–19.5 μm). The flux error bars are plotted if they are larger than the data points. The solid black line in each plot shows the best-fit YSO model (Robitaille et al. 2006). The acceptable YSO fits are shown in gray. The dashed line is the central stellar atmosphere corresponding to the best-fit model, extinguished by the fitted foreground extinction. The physical parameters estimated based on the YSO SED fitting are listed in Table 2. The source number given in Table 2 of Viehmann et al. (2006) followed by its near-IR identified name is shown on each plot.

Table 2
The SED Fitting Results: Physical Parameters of the YSO Candidates

V06	χ^2_{\min}/pt^a	n_{fits}^b	A_V		L_* ($10^4 L_\odot$)		T_* (10^4 K)		M_* (M_\odot)		M_{env} (M_\odot)		M_{disk} (M_\odot)		Evol. Stage		#
V0 ID			Best	Ave ^c	Best	Ave	Best	Ave	Best	Ave	Best	Ave	Best	Ave	Best	Ave	Data
5	1.36	367	25.0	25.3 (1.0)	2.4	1.1 (0.05)	3.21	2.74 (0.02)	15.9	11.7 (0.2)	0.00	0.15 (0.07)	0.000	0.006 (0.001)	III	II	6
6	1.33	31	25.0	25.0 (0.0)	7.1	6.0 (0.27)	3.76	3.66 (0.03)	23.7	22.1 (0.4)	0.00	0.0 (0.0)	0.043	0.130 (0.027)	II	II	9
10	0.53	5700	25.5	27.2 (2.4)	0.12	0.33 (0.01)	1.93	1.94 (0.01)	6.4	7.85 (0.03)	9.2	22.1 (1.8)	0.056	0.033 (0.001)	II	I	4
11	0.03	4583	29.8	27.7 (2.4)	0.32	0.37 (0.01)	0.51	1.88 (0.01)	10.6	8.55 (0.03)	1293	52.3 (3.3)	0.219	0.054 (0.002)	I	I	5
12	0.03	3039	29.2	28.3 (2.2)	0.49	0.46 (0.01)	0.41	1.98 (0.01)	11.9	9.21 (0.04)	1415	65.7 (4.8)	0.000	0.061 (0.002)	I	I	5
13	0.43	29	25.0	25.1 (0.6)	7.09	6.58 (0.51)	3.77	3.45 (0.05)	23.7	22.8 (0.8)	0.00	160 (114)	0.043	0.137 (0.028)	II	I	7
14	0.27	627	29.1	26.9 (2.2)	2.43	1.77 (0.04)	3.21	2.98 (0.01)	15.9	13.8 (0.1)	0.00	2.7 (1.5)	0.010	0.029 (0.003)	II	I	7
15	0.19	2192	29.9	26.8(2.2)	1.15	0.87 (0.01)	2.84	2.43 (0.01)	12.2	11.2 (0.1)	0.00	83.0 (7.2)	0.004	0.060 (0.003)	II	I	7
18	0.49	1245	25.0	26.7 (2.2)	0.94	1.28 (0.02)	2.75	2.75 (0.01)	11.4	12.2 (0.1)	0.00	21.8 (4.9)	0.066	0.042 (0.003)	II	I	7
19	0.06	5145	25.0	27.0 (2.3)	1.17	0.93 (0.01)	2.85	2.41 (0.01)	12.3	11.39 (0.03)	20.4	81.5 (3.2)	0.000	0.067 (0.002)	II	I	7
26	0.24	4954	25.0	27.6 (2.4)	0.21	0.17 (0.003)	0.43	1.66 (0.01)	10.1	6.40 (0.03)	33.7	13.8 (1.5)	0.040	0.026 (0.001)	I	I	5
28	1.85	776	25.0	25.1 (0.6)	1.21	1.61 (0.03)	2.81	2.92 (0.01)	12.0	13.2 (0.1)	0.00	0.0 (0.0)	0.038	0.016 (0.002)	II	II	8
31	1.98	193	25.9	26.3 (2.0)	2.76	3.16 (0.08)	3.27	3.31 (0.01)	16.6	17.2 (0.2)	0.00	0.0 (0.0)	0.000	0.034 (0.005)	II	II	7
32	2.37	547	25.0	25.3 (1.0)	2.68	1.96 (0.03)	3.25	3.00 (0.02)	16.4	14.6 (0.1)	0.00	24.4 (3.7)	0.018	0.037 (0.003)	II	I	9
39	0.80	879	30.0	27.8 (2.3)	1.62	1.33 (0.03)	0.41	2.57 (0.03)	23.9	12.7 (0.1)	408	87.8 (13.1)	0.221	0.056 (0.004)	I	I	5
47	1.32	186	30.0	27.8 (2.0)	4.62	2.84 (0.09)	3.52	3.23 (0.02)	20.0	16.4 (0.2)	0.00	0.0 (0.0)	0.068	0.016 (0.003)	II	II	9
48	0.36	565	30.0	27.5 (2.2)	3.86	1.98 (0.04)	3.39	3.04 (0.01)	18.1	14.3 (0.1)	0.00	0.7 (0.7)	0.052	0.027 (0.003)	II	II	8
54	0.48	19	25.0	25.0 (0.0)	7.09	6.63 (0.37)	3.76	3.70 (0.04)	23.7	22.9 (0.6)	0.00	0.0 (0.0)	0.043	0.176 (0.030)	II	II	9
57	0.77	2549	30.0	27.3 (2.2)	0.40	0.55 (0.01)	2.38	2.35 (0.082)	8.8	9.19 (0.04)	0.00	14.6 (1.8)	0.007	0.027 (0.001)	II	I	6

Notes.^a χ^2_{\min}/pt is a χ^2 per data point for the best-fit model.^b n_{fits} is a number of fits with χ^2/pt between χ^2_{\min}/pt and $\chi^2_{\min}/pt + 2$.^c The uncertainties represent standard deviations of the mean.

However, the *Herschel* PACS instrument (Poglitsch et al. 2010) had insufficient angular resolution ($\sim 5''$) at $70\ \mu\text{m}$ to resolve individual YSO candidates in this crowded field and in the presence of diffuse emission from the CMR. Despite this, for some sources, the generous upper limits that are derived, ranging between $(3.24\text{ and }5.75) \times 10^{-9}\text{ erg s}^{-1}\text{ cm}^{-2}$ for sources listed in Table 2, can rule out a few of the models with the most massive envelopes. Somewhat more restrictive upper limits (e.g., factors of 10 lower) would eliminate models with envelopes greater than $\sim 14 M_{\odot}$. Sources 10, 11, 26, and 39 would be most strongly impacted, changing them from likely Stage I objects to Stage II objects.

SED modeling of the infrared excess sources listed in Table 2 indicates that they are massive YSO candidates. In particular, the SED fits to members of the two complexes, IRS 5 and IRS 13N, are consistent with being massive YSO candidates. Four members of the IRS 5 Complex (IRS 5, IRS 5E, IRS 5S, and IRS 5SE1), as well as sources IRS 13N, IRS 13NE, IRS 2L, IRS 1W, and IRS 10W are classified as main-sequence or WR stars that may be associated with ionized streamers. Stellar sources in the IRS 5 Complex have been interpreted as low-luminosity bow shock sources, low-luminosity dust forming AGB stars, or YSOs (Preger et al. 2008). Based on proper motion measurements of cluster members in IRS 5 and IRS 13 as well as their high luminosities, these sources are unlikely to be AGBs and could be members of young cluster of stars (Preger et al. 2008; Eckart et al. 2013). The distribution of luminous YSO candidates imply that ongoing star formation is taking place near Sgr A* within the ionized streamers orbiting Sgr A* (e.g., Viehmann et al. 2006; YBWR08; Eckart et al. 2013; Nishiyama & Schödel 2013; Yusef-Zadeh et al. 2013, 2014; Jalali et al. 2014). Additional support for ongoing star formation within 2 pc of Sgr A* comes from radio continuum and near-IR polarization studies, as described below. Radio continuum observations did not detect a bow shock structure but resolved IRS 21 into at least four components (Yusef-Zadeh et al. 2014), suggesting that this a compact young stellar cluster. The radio emission from a cluster of four YSOs is due to thermal bremsstrahlung from ionized gas that is being photo-evaporated from a disk by the strong UV radiation field at the Galactic center.

In our sample of YSO candidates we include two sources that were not well fitted with the YSO models. These are IRS 1W and IRS 10W with $\chi^2_{\text{min}}/\text{of}$ 12 and 5, respectively. Their SEDs are shown separately in Figure 3. These sources are not included in Table 2 since the physical parameters estimated from the fitting are highly uncertain. However, other observations indicate that these sources are likely YSO candidates. IRS 1W and IRS 10W coincide within three clumps of SiO (5-4) emission 1, 2, and 3 (Yusef-Zadeh et al. 2013). SiO (5-4) line emission with broad line widths, as discussed in Section 3, provide strong support for protostellar outflows interacting with the ISM. Additional support comes from near-IR polarization measurements indicating that sources IRS 1W, IRS 10W, and IRS 21 are intrinsically polarized sources (Yoshikawa et al. 2013). Intrinsically polarized sources are argued to be associated with YSOs driven by outflows in star-forming regions (Yoshikawa et al. 2013). Table 3 gives the Viehmann et al. (2006) ID numbers (V06 ID), the corresponding near-IR names (Names), and equatorial coordinates for 19 well-fitted

YSO candidates, as well as sources IRS 1W and IRS 10W. Cross-references are provided for some of the sources.

Recent radio continuum observations within $30''$ of Sgr A* show evidence of partially resolved free-free emission from near-IR identified stellar sources, e.g., IRS 21, IRS 5, IRS 13N, and IRS 13E (Yusef-Zadeh et al. 2014). We argued that the radio emission is due to thermal bremsstrahlung from ionized gas that is being photo-evaporated from a disk by the strong UV radiation field at the Galactic center. In this picture, the mass-loss rate due to photo-evaporation implies the existence of a reservoir of neutral material. Robitaille et al. (2006) models consider envelope outer radii ranging between $\sim 1.5 \times 10^{16}$ and $\sim 1.5 \times 10^{18}\text{ cm}$. This range in size appears to be motivated by the limit at which the temperature would drop to 30 K. On the other hand, disk and inner envelope radii from our SED models range between 5 and 3000 AU (7.5×10^{13} and $4.5 \times 10^{16}\text{ cm}$). In the case of evolved stars in the Galactic center region, there is no identified AGB star that is detected at radio wavelengths. The outer radii of AGB stars can be as large as few $\times 10^{17}\text{ cm}$ (Wallerstein & Knapp 1998). If the envelope of AGBs or YSOs were photoionized, their angular size at the Galactic center would show extended radio sources greater than $1''$ ($1''$ is 0.04 pc at the distance of the Galactic center). One of the dustiest AGB sources in the Galactic center is IRS 3 (Preger et al. 2008), which shows no signature of extended thermal emission. Radio sources are partially resolved at $\sim 0''.1$ resolution. Thus, detection of partially resolved radio continuum sources in the Galactic center is consistent with SED models of infrared excess sources. Notable sources indicating a disk of material associated with YSO candidates are IRS 1W, IRS 5, IRS 5NE, IRS 13N, IRS 13NE, IRS 21, and IRS 34SW, corresponding to sources 1, 13, 14, 47, 48, 54, and 57 in Table 2.

Some of the stars, IRS 1W, IRS 10W, IRS 5, IRS 2L, and IRS 21, show bow shock structures with featureless SEDs that peak in mid-IR wavelengths (Tanner et al. 2002, 2005; Clenet et al. 2004; Muzic et al. 2010; Sanchez-Bermudez et al. 2014). The bow shock morphologies of these sources are interpreted in terms of the interaction of ionized winds with the streamers of ionized gas (Tanner et al. 2005; Sanchez-Bermudez et al. 2014). This model adopts a spherical outflow from central Wolf-Rayet stars (Tanner et al. 2002, 2005). Alternatively, the interaction of ionized streamers could take place with the material evaporating from the YSO disks assuming that the outflow from the YSO disks is faster than the relative motion between the YSOs and the ionized streamers. In this scenario, the cause of the asymmetry comes from the outflow arising preferentially from the disk surface, facing the ionizing sources in the central cluster of stars. The asymmetry in the bow shock geometry could also come from YSO disks interacting with ionized streamers. The orientation of YSO disks should be random in the disk picture. The orientations of the bow shock in IRS 10W, IRS 5 do not seem to follow the north-south direction of the streamers, which is consistent with disks associated with YSO candidates.

YSO candidates' stellar masses derived from the SED fitting can be used to estimate the star formation rate (SFR; e.g., Whitney et al. 2008; Yusef-Zadeh et al. 2009; Povich et al. 2011). The SFR is calculated by estimating the total mass of the YSO candidates and dividing it by the YSOs' approximate lifetime. Since our sample of YSO candidates is small, we can

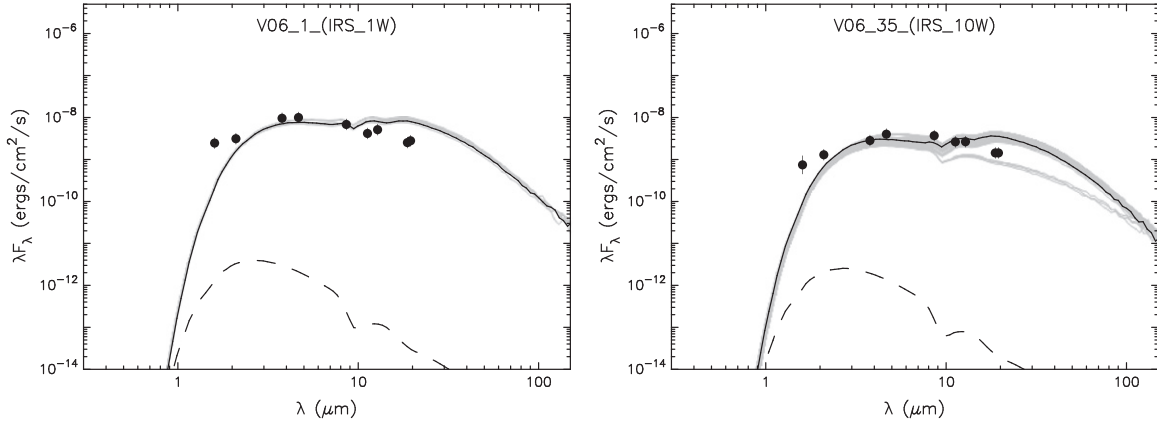


Figure 3. Similar to Figure 2 except that SED YSO model fits to IRS 1W and IRS 10W, as presented in the left and right panels, give χ^2/pt that are 12 and 5, respectively. The YSO-fitted SEDs to these sources are more uncertain than those shown in Figure 2.

Table 3
YSO Candidate Positions and Literature References

V06 ID	Other Name	R.A. (J2000)	Decl. (J2000)	Cross-reference
1	IRS 1W	17 45 40.44	−29 00 27.7	1, 3, 6, 8
5	...	17 45 40.46	−29 00 29.2	
6	IRS 2L	17 45 39.78	−29 00 32.1	8, 9
10	...	17 45 39.98	−29 00 24.3	...
11	IRS 4	17 45 40.84	−29 00 34.2	...
12	...	17 45 40.80	−29 00 37.0	...
13	IRS 5	17 45 40.70	−29 00 18.5	1, 4, 5, 6, 8
14	IRS 5NE	17 45 41.02	−29 00 17.7	5, 8
15	IRS 5E	17 45 40.87	−29 00 19.0	5
18	IRS 5S	17 45 40.74	−29 00 20.3	5
19	IRS 5SE1	17 45 40.86	−29 00 21.3	5
26	...	17 45 40.03	−29 00 20.4	...
28	...	17 45 40.33	−29 00 21.1	...
31	...	17 45 40.32	−29 00 33.6	...
32	...	17 45 40.36	−29 00 35.6	...
35	IRS 10W	17 45 40.54	−29 00 23.1	1, 2, 6, 8
39	...	17 45 40.52	−29 00 31.1	...
47	IRS 13N	17 45 39.81	−29 00 29.2	7, 10
48	IRS 13NE	17 45 39.84	−29 00 29.7	7
54	IRS 21	17 45 40.22	−29 00 31.0	1, 2, 4, 8, 11
57	IRS 34SW	17 45 39.74	−29 00 26.7	...

References. (1) Sanchez-Bermudez et al. (2014), (2) Yoshikawa et al. (2013), (3) Paumard et al. (2006), (4) Tanner et al. (2002), (5) Preger et al. (2008), (6) Tanner et al. (2005), (7) Eckart et al. (2013), (8) Buchholz et al. (2013), (9) Moutaka et al. (2004), (10) Muzic et al. (2010), and (11) Yusef-Zadeh et al. (2014).

only provide a rough approximation of the SFR. We use Stage I (the average evolutionary stage from Table 2) YSO candidates only to get a sample of sources at approximately the same age and lifetime.

To estimate the total mass of the YSOs, we construct the stellar mass function, scale the Kroupa (2001) initial mass function (IMF; $dN/dm \propto m^{-\alpha}$, where m is a stellar mass) to match the peak of the distribution, and integrate under the IMF over a mass range of $0.08\text{--}50 M_{\odot}$. The Kroupa (2001) IMF has a slope (α) of 1.3 between 0.08 and $0.5 M_{\odot}$ and 2.3 between $0.5 M_{\odot}$ and $50 M_{\odot}$. The estimated total mass of the YSO candidates is $\sim 1318 M_{\odot}$. Assuming a typical lifetime of the Stage I YSO of 10^5 yr, the SFR within 1 pc of Sgr A* is estimated to be $\sim 1 \times 10^{-2} M_{\odot} \text{ yr}^{-1}$. This is only an order magnitude estimate because of the small number statistics,

uncertainty of a factor of two in the age of Stage I YSOs (see Koepferl et al. 2015), and the extrapolation of the IMF down to the cut-off at $0.08 M_{\odot}$.

3.2.1. YSO Candidates in Rotating Disks Orbiting Sgr A*

One of the most intriguing aspects of the YSO candidates is their spatial distribution, which appears to be similar to that of the young, hot stars orbiting Sgr A*. The so-called edge-on clockwise and face-on counterclockwise stellar disks have positive and negative angular momentum j , respectively (Beloborodov et al. 2006; Paumard et al. 2006) and consist of hot and massive stars which are a few million years old (Paumard et al. 2006; Lu et al. 2009). The two disks extend out to $10''$ from Sgr A*. The position angles (PAs) of young stars in the clockwise and counterclockwise stellar disks are $\sim 30^\circ$ and 130° , respectively. Figures 4(a) and (b) show the positions of YSO candidates superimposed on a 34 GHz continuum and $3.8 \mu\text{m}$ images, respectively. YSO candidates IRS 5, source 28, and IRS 2L are embedded or offset to the east of the N arm of the ionized mini-spiral, IRS 4 and source 12 lie in the E arm, and IRS 13E, IRS 13N, and IRS 34SW lie in projection against the bar of ionized gas and its NW extension. The YSO candidates that are distributed diagonally from NE to SW run parallel to the face-on counterclockwise disk whereas the sources to the SE fall along the clockwise stellar disk. The distributions of YSOs extend to $\sim 15''$ from Sgr A*, larger than the $10''$ extent of counter-rotating disks. The three-dimensional motions of many of the YSO candidates are unknown; however, the line of sight motion of the YSO candidates and their apparent distribution on the sky show a trend that is consistent with the positive and negative angular momenta of two rotating disks. For example, the proper motion of the IRS 5S1 to 3 clusters suggest that the overall angular momenta of these sources is in agreement with the clockwise rotating disk of stars (Preger et al. 2008). In addition, IRS 34SW has positive angular momentum, and thus follows clockwise rotating disks whereas IRS 13 has negative angular momentum values. This suggests that the YSO candidates are forming in the residual outer regions of the original gas disks that formed the original stellar disks orbiting Sgr A*. Future proper motion measurements will determine the angular momentum of the YSO candidates and test the picture proposed here.

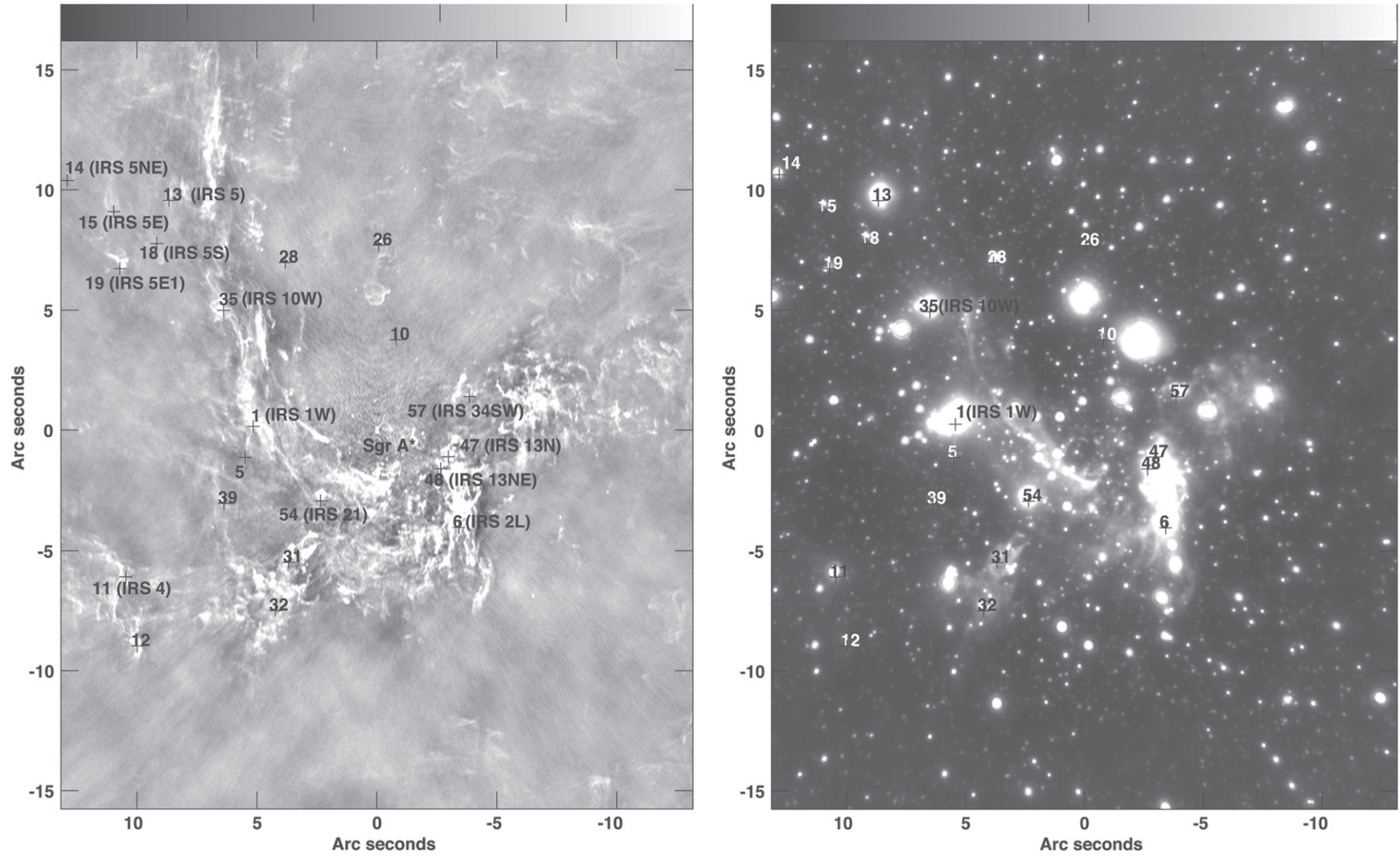


Figure 4. (a) Distribution of YSO candidates, as listed in Table 2 superimposed on a 34 GHz continuum image based on a VLA A-array observation with a resolution of $0''.089 \times 0''.046$ ($\text{PA} = -1^\circ 56'$) (F. Yusef-Zadeh et al. 2015, in preparation). (b) Same as (a) except for an L-band ($3.8 \mu\text{m}$) image using the VLT.

Table 4
Gaussian Line Parameters of Fitted SiO (5-4) Sources

Source	R.A. (J2000)	Decl. (J2000)	Peak Intensity (mJy beam ⁻¹)	Center Velocity (km s ⁻¹)	FWHM (km s ⁻¹)	FWZI (km s ⁻¹)
10	17:45:40.31	-29 00 43.77	174.7 ± 20.0	-58.88 ± 1.87	33.43 ± 4.41	68 ± 20
10 (ALMA)	71.32 ± 2.75	-42.98 ± 0.39	21.02 ± 0.95	56 ± 18
12	17:45:41.08	-29 00 37.46	91.58 ± 19.3	-10.60 ± 5.34	51.68 ± 12.6	96 ± 15
13	17:45:40.69	-29 00 45.83	238.9 ± 28.2	-36.61 ± 0.96	17.65 ± 2.52	35 ± 10
14	17:45:40.37	-29 00 53.73	263.2 ± 19.0	-54.42 ± 0.99	28.11 ± 2.34	49 ± 14
15	17:45:40.20	-29 01 00.20	557.9 ± 34.9	-74.76 ± 1.06	34.67 ± 2.50	159 ± 40
16	17:45:39.78	-29 01 05.94	450.1 ± 26.3	-76.72 ± 0.98	34.14 ± 2.30	62 ± 8
17	17:45:41.32	-29 01 01.63	317.3 ± 32.1	10.83 ± 1.11	12.71 ± 1.56	27 ± 5
18	17:45:41.55	-29 00 57.08	312.9 ± 16.9	9.424 ± 0.80	10.86 ± 0.92	14 ± 10
19	17:45:41.84	-29 00 57.56	317.4 ± 10.6	11.12 ± 4.09	9.842 ± 4.94	14 ± 8
20	17:45:44.85	-29 00 25.25	282.3 ± 31.0	36.61 ± 0.89	17.70 ± 2.35	27 ± 5
21	17:45:43.73	-29 00 16.63	327.0 ± 57.9	35.85 ± 0.88	15.09 ± 3.44	23 ± 5
22	17:45:43.52	-29 00 07.06	524.3 ± 26.9	43.76 ± 0.63	24.97 ± 1.48	46 ± 12
23	17:45:43.74	-28 59 59.88	341.8 ± 39.5	39.34 ± 1.61	28.56 ± 3.81	55 ± 10
24	17:45:41.75	-28 59 47.62	316.1 ± 34.2	87.37 ± 0.96	18.11 ± 2.28	34 ± 8
25	17:45:39.49	-28 59 51.02	268.6 ± 30.6	10.17 ± 1.90	34.06 ± 4.48	65 ± 20
26	17:45:39.31	-29 00 02.95	182.8 ± 24.2	28.15 ± 1.71	26.37 ± 4.04	51 ± 15
27	17:45:39.14	-29 00 16.74	227.5 ± 36.8	37.35 ± 1.68	21.22 ± 3.97	40 ± 13
28	17:45:38.17	-29 00 33.00	225.2 ± 20.8	12.76 ± 0.93	20.63 ± 2.21	39 ± 10
29	17:45:38.46	-29 00 33.68	243.3 ± 10.5	61.78 ± 1.52	25.25 ± 3.24	45 ± 20
30	17:45:37.44	-29 00 44.36	153.1 ± 21.8	-23.25 ± 2.76	39.52 ± 6.59	56 ± 15
31	17:45:38.25	-29 00 41.49	505.5 ± 34.8	-29.03 ± 1.00	29.60 ± 2.35	58 ± 20
32	17:45:38.37	-29 00 48.61	575.9 ± 60.1	-39.59 ± 2.58	50.49 ± 6.09	92 ± 25
33	17:45:37.97	-29 00 48.47	597.3 ± 34.2	-46.93 ± 1.50	53.55 ± 3.54	108 ± 25
34	17:45:38.04	-29 00 54.08	479.0 ± 32.2	-39.21 ± 1.34	40.76 ± 3.17	84 ± 18
35	17:45:38.46	-29 01 02.71	611.5 ± 3.63	-124.3 ± 0.12	36.57 ± 0.31	80 ± 50
36	17:45:39.04	-29 01 03.39	206.6 ± 18.6	-100.5 ± 1.08	24.46 ± 2.54	51 ± 15
37	17:45:35.88	-29 01 08.01	178.1 ± 31.2	-40.70 ± 2.32	27.01 ± 5.46	41 ± 20

3.3. Protostellar Outflows Traced by SiO Emission

Another indication that the region within 0.5 pc of Sgr A* is a site of ongoing star formation comes from clumps of SiO emission found in this region (Yusef-Zadeh et al. 2013). ALMA observations of the interior of the molecular ring detected 11 clumps of SiO (5-4) emission within the inner 0.5 pc of Sgr A*. SiO line emission is generally associated with shocks from protostellar outflows, so SiO clumps detected within the molecular ring were interpreted as evidence of young star formation activity near Sgr A* where outflows from YSOs interact with the surroundings. The location of five SiO clumps are offset from the eastern edge of the N arm but run parallel along the N arm of ionized gas. These sources show typical line widths between 11 and 21 km s⁻¹ and peak radial velocities that decrease from 37.8 to 7.4 km s⁻¹ to the N of the streamers. This trend in radial velocity is consistent with the trend in the kinematics of ionized gas of the N arm (e.g., Zhao et al. 2010). However, the radial velocity distribution of the SiO clumps does not match the kinematics of ionized gas in the N arm. The positions of two of the most prominent SiO (5-4) clumps found by ALMA (sources 1 and 11 in Yusef-Zadeh et al. 2013) lie along the extension of YSO candidates found to the NE of where the IRS 5 cluster is located. This suggests that there is a concentration of molecular gas to the east of the N arm.

We extended the study of SiO (5-4) line emission from the inner 0.5 pc to the molecular ring within ~2 pc of Sgr A* using data taken with the SMA with a resolution of 3".6 × 2".4 (Martin et al. 2012). Table 4 lists the parameters of Gaussian fitted SiO (5-4) line emission found in the molecular ring.

Columns 1–7 show the source number, following the SiO (5-4) sources detected by ALMA (Yusef-Zadeh et al. 2013), celestial coordinates, peak intensity, FWHM, and full width at zero intensity (FWZI), respectively. The SiO (5-4) sources detected by ALMA are concentrated in a region within the molecular ring where SMA observations could not detect any SiO (5-4) line because of its poor sensitivity with the exception of source 10, which was detected in both ALMA and SMA observations. Table 4 shows that the parameters of the fit to this source detected with ALMA and SMA are similar to each other. The discrepancy between the fitted parameters of SMA source 10 and 10 (ALMA) in Table 4 is mainly due to different spatial and spectral resolutions and the sensitivity of the ALMA and SMA data.

Figure 5 shows the velocity-integrated SiO (5-4) line intensity of 26 clumps toward the molecular ring. To investigate if these new SiO clumps have similar characteristics to known protostellar outflows in the Galactic disk, Figure 6(a) compares the line widths and SiO (5-4) luminosity of the emission from 11 clumps interior to the ring (red), found from ALMA observations, 26 clumps (12–36) in the molecular ring listed in Table 4 (blue) as well as low- and high-mass protostars in the Galactic disk (black). The SiO sources lying in the central hole in the central molecular ring as well as the clumps coincident with the ring show a similar lack of dependence between the FWZI and SiO luminosity found for high-mass protostellar systems in the Galactic disk (Yusef-Zadeh et al. 2013). This supports the suggestion that the SiO clumps in the CMR are massive protostellar outflows and the CMR itself is a site of recent massive star formation. We note a

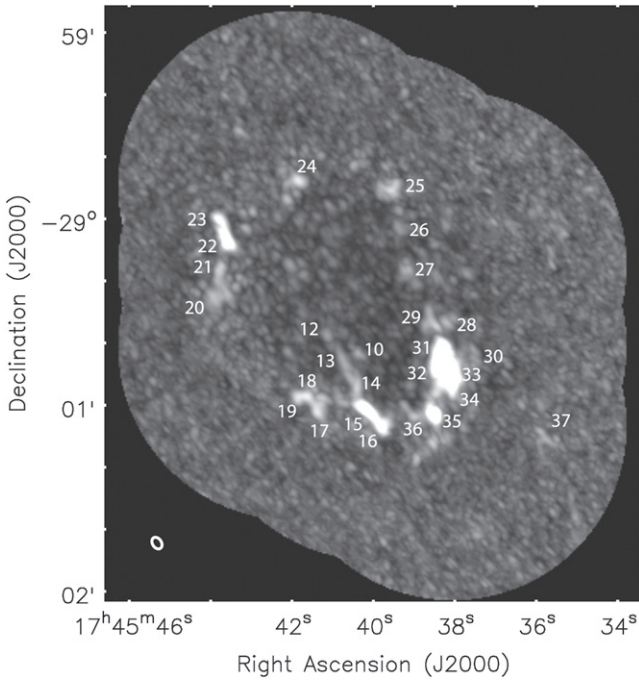


Figure 5. Map of SiO (5-4) line emission from the molecular ring with a resolution of $3''.6 \times 2''.4$. Individual SiO (5-4) clumps, as listed in Table 4, are labeled. The SiO (5-4) data were originally published in Martin et al. (2012). Clump F in the HCN map of the molecular ring (Christopher et al. 2005) coincides with SiO (5-4) clumps 23 and 24.

bipolar outflow candidate (Figure 6(b)) in one of the SiO clumps, as described below.

3.3.1. SiO (5-4) Bipolar Outflow

One of the clearest signatures of ongoing star formation activity is bipolar outflows traced by SiO line emission. We identified a bipolar outflow candidate in clump F or clumps 22 and 23 in Figure 5 of the CMR. The reason that we were able to identify this source is because the F clump is less confused kinematically and spatially than the material in the molecular ring. Figure 6(b) shows contours of SiO (5-4) line intensity for a velocity range between 30 and 55 km s^{-1} (blue) and 65–90 km s^{-1} (red). The kinematics of SiO (5-4) line emission show the appearance of a bipolar outflow from clumps 22 and 23. The spectrum of this source shows broad blue and redshifted wings and the blue and redshifted radial velocities along the linear features are reminiscent of bipolar outflows. The direction of the velocity gradient of bipolar lobes is the opposite to that seen in the molecular ring (Christopher et al. 2005). The presence of methanol and water masers and bipolar outflow in the vicinity of clump F provides the strongest evidence for ongoing star formation in the molecular ring.

3.3.2. LVG Analysis of SiO Lines

In order to apply an LVG analysis to the sources detected in the SiO (5-4) and (2-1) lines, we first convolved the CARMA and SMA data to an identical resolution of $6''.85 \times 3''.73$ and then performed Gaussian fits to the sources, obtaining the parameters listed in Table 5. The CARMA sensitivity of SiO (2-1) was not sufficient to detect source 12. In addition, SiO (5-4) and SiO (2-1) data from SMA and CARMA showed some

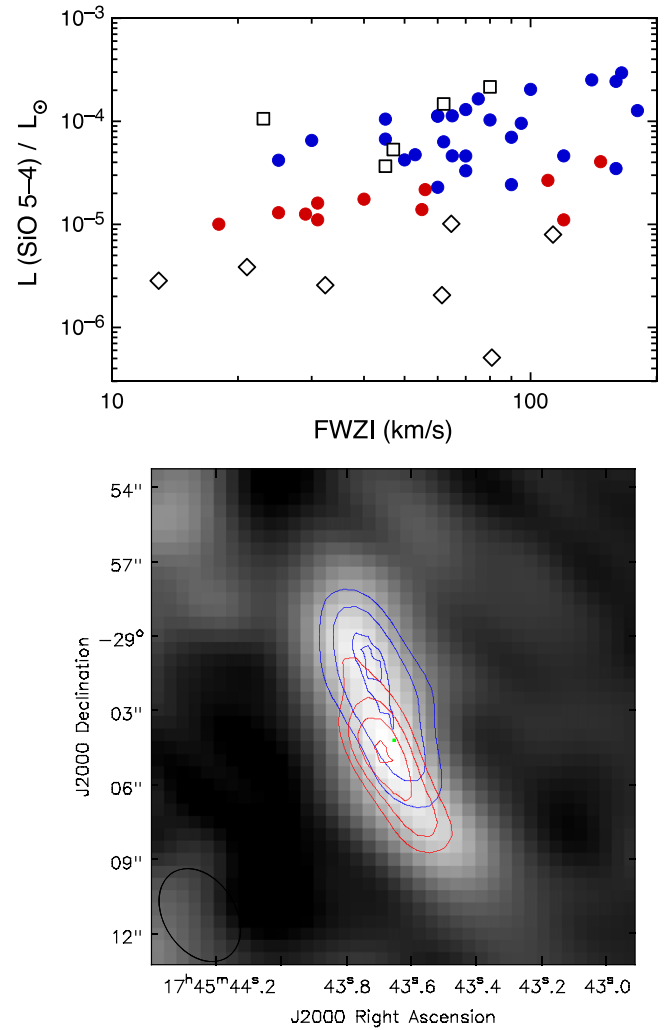


Figure 6. Top: the SiO (5-4) luminosity vs. the total line widths FWZI of the line emission toward 11 clumps in the molecular ring (red) based on ALMA observations, and 26 clumps in the molecular ring based on this work (blue) as well as low- and high-mass protostars in the Galactic disk (black diamonds and squares, respectively). Bottom: contours of SiO (5-4) line intensity between 30 and 55 km s^{-1} (blue) and 65–90 km s^{-1} (red) are superimposed on a grayscale image showing the integrated SiO (5-4) line emission from clumps 22 and 23 (Clump F in Christopher et al. 2005). The ellipse at the bottom left corner represents the spatial resolution of SMA data $3''.6 \times 2''.4$.

clumps with multiple velocity components. The LVG analysis adopted a uniform slab geometry for the emitting region, and included a radiation field characterized by a dust temperature of 75 K, 30 mag of visual extinction, and a dust extinction curve following Draine & Lee (1984). We computed the emergent intensities in the two lines given the slab's assumed gas density, temperature, FWHM velocity, and SiO column. In Figure 7, we show contours of 5-4 versus 2-1 brightness temperature for constant hydrogen number density (n_H) and for fixed SiO column density, assuming a FWHM of 30 km s^{-1} for kinetic temperatures of 150 K. Also plotted are the points corresponding to the observed SiO sources, which lie close to and follow contours within $n_H = 10^6$ or $n(\text{H}_2) \sim 5 \times 10^5$ and $10^{6.15} \text{ cm}^{-3}$ for the assumed kinetic temperature of 150 K. These estimates are similar to those given by Amo-Baladron et al. (2009). Note that the predicted brightness temperatures scale linearly with SiO column density because the lines are optically thin. We conclude that the sources have $n_H \approx$

Table 5
Gaussian Line Parameters of Fitted SiO (5-4) and (2-1) Sources

	Peak (mJy beam ⁻¹)	CARMA Center (km s ⁻¹)	FWHM (km s ⁻¹)	Peak (mJy beam ⁻¹)	SMA Center (km s ⁻¹)	FWHM (km s ⁻¹)
10	45.2 ± 64.2	-40.8 ± 3.2	46.8 ± 7.6	167.2 ± 18.3	-41.8 ± 1.3	24.2 ± 3.0
12	218.8 ± 10.1	-9.4 ± 1.7	74.4 ± 4.0
13	87.3 ± 13.2	-19.2 ± 3.2	61.1 ± 11.0	353.2 ± 23.6	-18.2 ± 0.7	23.7 ± 1.8
14	116.0 ± 8.7	-38.4 ± 1.1	32.0 ± 2.7	352.9 ± 20.9	-35.8 ± 0.9	31.0 ± 2.1
15	131.7 ± 9.6	-50.8 ± 1.5	43.1 ± 3.6	488.9 ± 23.8	-49.0 ± 1.0	42.2 ± 2.3
16	162.0 ± 9.9	-60.0 ± 0.7	26.4 ± 1.8	461.8 ± 39.5	-58.4 ± 1.1	26.3 ± 2.6
17	20.2 ± 12.7	27.2 ± 0.6	21.4 ± 1.5	420.7 ± 44.6	30.5 ± 0.6	12.0 ± 1.4
18	230.9 ± 12.1	30.7 ± 0.4	16.4 ± 1.0	395.6 ± 20.9	30.7 ± 0.3	13.3 ± 0.8
19	244.7 ± 12.7	28.0 ± 0.2	10.4 ± 0.6	403.4 ± 46.2	28.5 ± 0.5	10.1 ± 1.3
20	83.6 ± 15.9	37.8 ± 0.9	10.3 ± 2.2	158.0 ± 198.4	33.4 ± 3.4	6.6 ± 10.1
21	222.2 ± 11.3	57.1 ± 0.5	23.3 ± 1.4	532.1 ± 54.5	54.11 ± 0.7	14.6 ± 1.7
22	238.6 ± 9.7	62.7 ± 0.5	26.7 ± 1.3	631.2 ± 39.5	61.8 ± 0.7	25.4 ± 1.8
23	222.9 ± 7.9	63.7 ± 0.5	31.3 ± 1.3	683.7 ± 41.1	59.1 ± 0.7	25.8 ± 1.8
24	120.1 ± 10.1	104.0 ± 0.8	20.3 ± 1.9	254.2 ± 22.2	107.1 ± 0.8	20.4 ± 2.0
25	71.5 ± 5.4	38.2 ± 2.0	54.5 ± 4.7	320.5 ± 17.1	32.0 ± 1.1	43.1 ± 2.6
26	70.7 ± 9.7	48.4 ± 1.8	26.6 ± 4.2	137.9 ± 21.0	42.5 ± 1.9	25.6 ± 4.5
27	77.6 ± 8.4	61.9 ± 1.5	28.2 ± 3.5	265.2 ± 25.1	60.4 ± 1.1	24.1 ± 2.6
	14.86 ± 11.2	-13.9 ± 1.9	50.8 ± 4.6
28	68.9 ± 5.9	34.1 ± 0.8	20.2 ± 2.0	190.6 ± 22.9	35.9 ± 1.4	24.9 ± 3.4
	49.6 ± 8.4	87.5 ± 2.0	24.3 ± 4.8	111.6 ± 17.9	87.8 ± 1.7	22.4 ± 4.2
29	128.1 ± 5.9	82.8 ± 0.5	23.5 ± 1.2	307.1 ± 37.6	84.8 ± 1.3	21.5 ± 3.2
30	36.3 ± 6.4	-11.5 ± 4.4	51.5 ± 10.5
31	199.1 ± 6.4	-11.7 ± 0.6	37.3 ± 1.4	613.3 ± 25.1	-10.8 ± 0.6	34.4 ± 1.6
32	228.7 ± 9.5	-22.6 ± 1.0	53.5 ± 2.5	730.6 ± 26.4	-19.5 ± 0.9	54.4 ± 2.2
33	250.5 ± 8.7	-22.4 ± 0.9	56.4 ± 2.2	831.9 ± 21.8	-23.1 ± 0.7	58.5 ± 1.7
34	211.8 ± 9.2	-23.3 ± 1.1	52.3 ± 2.6	807.3 ± 21.8	-22.3 ± 0.6	50.8 ± 1.5
35	152.9 ± 10.6	-104.6 ± 1.1	34.6 ± 2.7	620.2 ± 15.7	-103.4 ± 0.4	37.5 ± 1.1
36	64.5 ± 11.9	-81.7 ± 1.1	12.5 ± 2.6	183.6 ± 27.2	-79.3 ± 1.4	20.1 ± 3.4
	116.5 ± 34.1	-4.6 ± 3.1	2.20 ± 7.5
37	107.4 ± 11.6	-19.4 ± 1.3	24.9 ± 3.2	444.4 ± 42.9	-17.2 ± 1.1	24.4 ± 2.7

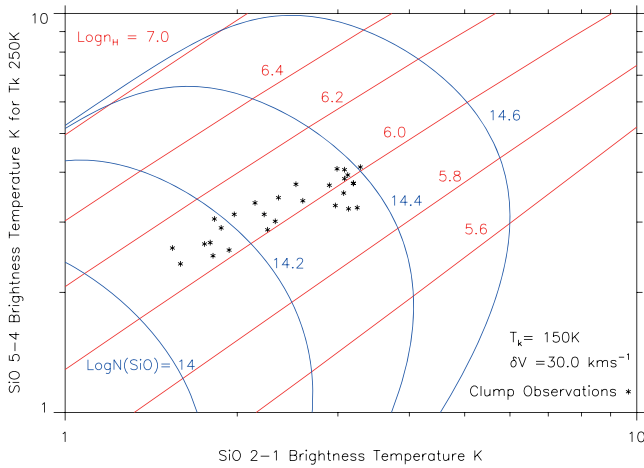


Figure 7. Intensities in the SiO (5-4) vs. SiO (2-1) lines for an assumed kinetic temperature of 150 K and FWHM (δv) of 30 km s⁻¹. Blue and red colors represent contours of constant SiO column density and gas density, respectively. The black star symbols coincide with the observed brightness of SiO (5-4) and (2-1) clumps.

$1-4 \times 10^6 \text{ cm}^{-3}$ for assumed kinetic temperatures of 50 and 150 K and $N(\text{SiO}) \approx 10^{14.4} \text{ cm}^{-2}$. As with other linear molecules, we find that the density inferred from the LVG analysis is inversely proportional to the assumed kinetic temperature, so that the LVG constrains the pressure in the SiO sources to be $P/k \approx 1 \times 10^8 \text{ K cm}^{-3}$.

The SiO clumps are interpreted to be arising from protostellar outflow sources. Using a typical molecular density $\sim 10^6 \text{ cm}^{-3}$ and a radius of $\sim 2''$, the total mass that is swept up a molecular clump of SiO emission by protostellar outflow is estimated to be $\sim 68 M_{\odot}$. The kinetic luminosity $L_{\text{kinetic}} = 0.5 \text{ Mv}^2$ of the swept-up material over the dynamical age ~ 1300 years is also calculated to be $\sim 500 L_{\odot}$. Using the estimated SiO and molecular hydrogen column densities, the abundance of SiO in each SiO clump is estimated to be 2.5×10^{-10} . The column density of hydrogen itself is estimated by multiplying the gas density and the size of a clump. However, SiO shocks are generally associated with a thin layer where the protostellar jet interacts with a cloud. So, we overestimated the thickness of the SiO layer by a factor of 10 to 100 and therefore underestimated the SiO abundance. Thus, the SiO abundance could range between 2.5×10^{-9} and 2.5×10^{-8} .

3.3.3. Water Maser, HCN, and SiO Lines

To investigate whether water masers (see Figure 1) are tracking star formation activity, we compare the distribution of SiO (5-4) emission with the spectra of several water masers toward the molecular ring. Figure 8 shows a grayscale image of SiO (5-4) line emission from the molecular ring and the insets show six SiO (5-4) spectra from regions where water masers have been detected. Water masers 1, 11, and 12 lie in the vicinity of HCN(1-0) clumps F and G, whereas water masers 4 and 5 are concentrated near HCN (1-0) clump O. These SiO features associated with clumps F, G, and O to the E and SW of

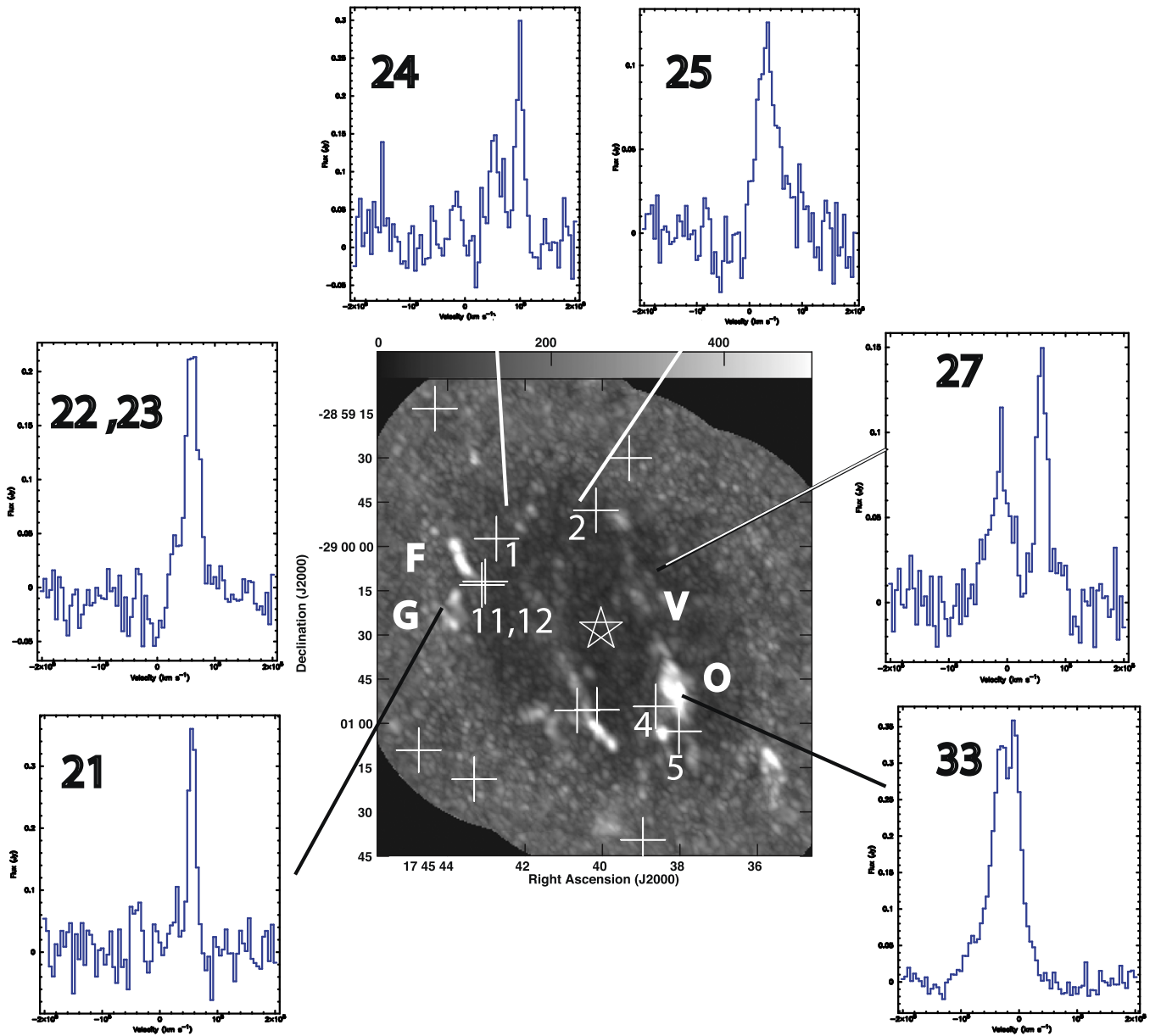


Figure 8. Grayscale image of SiO (5-4) line emission with a spatial resolution is $3''.6 \times 2''.4$. The spectra of SiO (5-4) line emission from six SiO (5-4) clumps, 21, 22 +23, 24, 25, 27, and 33 (see Figure 5), are displayed as insets. The crosses coincide with the location of water masers. HCN (1-0) Clumps F, G, V, and O are labeled (Christopher et al. 2005). The location of Sgr A* is shown by an asterisk. The velocity range of individual plots is between -2×10^5 and 2×10^5 km s $^{-1}$.

the molecular ring are resolved spatially in the N-S direction. The SiO (5-4) spectra 21 to 24 from the HCN (1-0) clumps F and G reveal velocities peaking between 30 and 60 km s $^{-1}$. These velocities are generally consistent with those of water masers 1 and 12. The velocity profile of SiO (5-4) from clump V shows two blue and redshifted velocity components whereas HCN (1-0) spectra show a broad asymmetric redshifted wing. SiO (5-4) line emission from Clump O shows a velocity peak at ~ -8 km s $^{-1}$ and extends to negative velocity of -100 km s $^{-1}$. The broad line width of this clump includes the LSR velocities of water masers 4 and 5. The spectra of SiO (5-4) line emission from clump O exhibit an asymmetric blueshifted wing.

Previous H $_2$ observations of the molecular ring (Gatley et al. 1986; Yusef-Zadeh et al. 2001) have identified shocked H $_2$ features associated with clumps V and O. The

correspondence between SiO, HCN(1-0), and H $_2$ molecular line emission suggests that H $_2$ emission from the CMR is shock excited. The velocity profiles of SiO emission are similar to those of HCN, thus suggesting that SiO (5-4) and HCN (1-0) line emission arise from the same region. In addition, velocities of water masers 1, 12, 4, and 5 are within the range of SiO emission from clumps F, G, and O, thus suggesting that these water masers may be associated with the molecular gas in the ring.

3.4. [Ne II] Line Emission

Figure 9(a) shows contours of HCN (1-0) line emission at the peak velocity of clump V superimposed on a grayscale continuum image of the mini-spiral H II feature at 5 GHz (Yusef-Zadeh & Wardle 1993). A radio continuum ionized

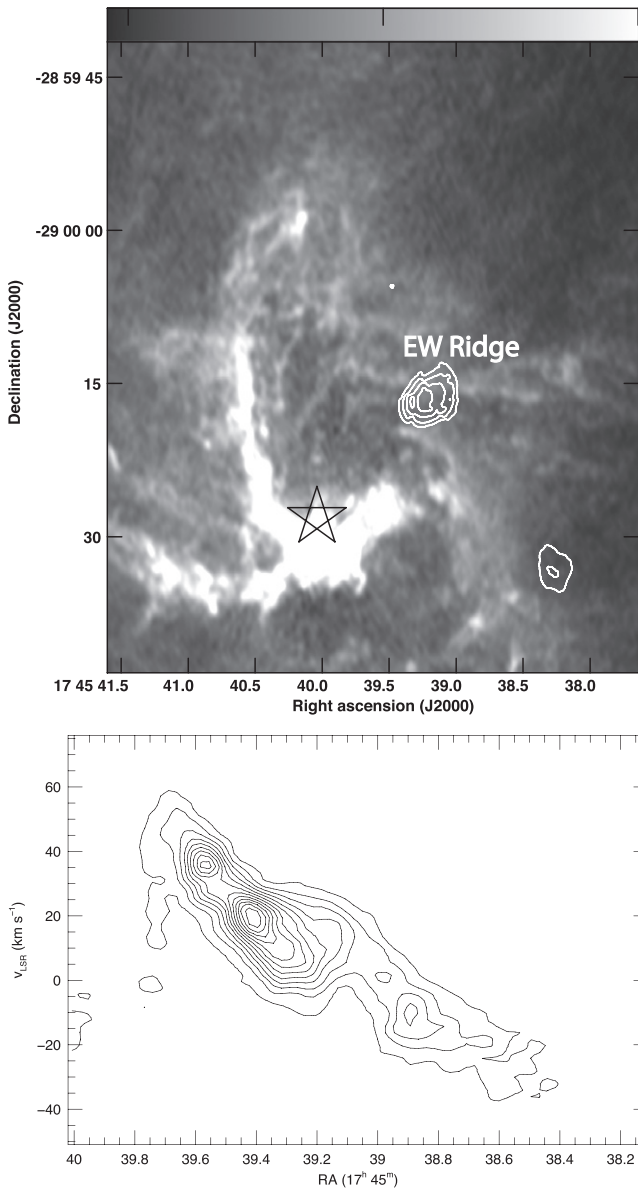


Figure 9. Top: contours of HCN(1-0) line emission from clump V are set at 3, 3.4, 3.8, and 4.2 Jy km s^{-1} and are superimposed on a 5 GHz continuum image (Yusef-Zadeh & Wardle 1993). A $20''$ horizontal structure EW Ridge with constant declination crosses contours of HCN emission from clump V and is noted on the grayscale 5 GHz image. The asterisk symbol corresponds to the location of Sgr A*. Bottom: the position-velocity diagram of [Ne II] line emission from the EW Ridge. The cut runs along the brighter branch of the EW ridge, at $\text{PA} \approx -93^\circ$.

feature, which we refer to as the EW Ridge, extends away from clump V at roughly constant declination. This ridge of ionized gas branches into two linear features, each with a horizontal and vertical extent of $\sim 20''$ (0.8 pc) and $1''$ (0.04 pc), respectively, crossing each other with PAs of 81° and 105° at the peak of clump V peaks. The kinematics of this feature do not follow the kinematics of the molecular ring. Morphologically, the linear features wiggle to the east as they merge with the N arm of the mini-spiral. Figure 9(b) shows the position-velocity (P-V) contour plot of [Ne II] line emission along the brighter branch along the length of the EW ionized ridge at a PA of -93° at almost constant declination. This plot illustrates the gradual change in the velocity of the linear feature from ~ 55 to -55 km s^{-1} with a velocity gradient of $\sim 470 \text{ km s}^{-1} \text{ pc}^{-1}$. The

red and blueshifted velocity components are associated with the eastern and western halves of the crossed linear features, respectively. Given the high-velocity gradient of Ne II line emission, the ionized gas associated with the EW ridge is kinematically disturbed and is likely to be unbound to the Galactic center gravitational potential. The blue- and redshifted radial velocities along the linear features are reminiscent of bipolar outflows.

We suggest that the EW feature is a result of jet activity from two protostars in clump V. A collisionally excited methanol maser is associated with clump V (YBRW08), at a velocity of $\sim 40 \text{ km s}^{-1}$, superimposed on broad thermal line emission extending to velocities of $\sim 80 \text{ km s}^{-1}$. There is no evidence of water masers arising from clump V. The dynamical age of the outflow is estimated to be $\sim 1 \times 10^4$ years using the size of the ionized ridge $\sim 20''$ (0.78 pc) and the difference in the blue and redshifted velocities $\sim 80 \text{ km s}^{-1}$. The intensity of the emission from the EW Ridge is $\sim 0.5 \text{ mJy beam}^{-1}$ at 22.4 GHz with a resolution of $0''.24 \times 0''.17$. The background subtracted flux density of the ionized EW Ridge is estimated to be $\sim 0.5 \pm 0.2 \text{ Jy}$ at 22.4 GHz. The ionized gas is estimated to have an emission measure $\text{EM} \sim 6 \times 10^6 \text{ pc cm}^{-6}$ corresponding to an ionized gas density of $8.7 \times 10^3 / f^{0.5} \text{ cm}^{-3}$ where f is the volume filling factor. The electron temperature is assumed to be $T_e \sim 8000 \text{ K}$ and a path-length $L = 0.08 \text{ pc}$, which is equivalent to the jet diameter $\sim 2''$. The total mass of the EW Ridge and the mass-loss rate of the outflowing ionized material are estimated to be $\sim 1.7 \times f^{0.5} M_\odot$ and $\sim 1.8 \times f^{0.5} \times 10^{-4} M_\odot \text{ yr}^{-1}$, respectively. Assuming 10% lumpiness in the density of ionized gas, $f = 0.1$, the total mass and the mass-loss rate are $\sim 0.5 M_\odot$ and $\sim 5 \times 10^{-5} M_\odot \text{ yr}^{-1}$, respectively. These values are generally consistent with those found in star-forming regions.

3.5. Radio Dark Clouds within 1 pc of Sgr A*

Star formation activity within the inner 2 pc of Sgr A* requires a reservoir of molecular gas surrounding the sites of young star-forming activity. The CMR provides the largest concentration of molecular gas near Sgr A*. Recent observations have also shown additional molecular material is distributed within the CMR, contrary to the widely accepted idea that a cavity of mini-spiral shaped ionized gas fills inside the molecular ring (Jackson et al. 1993; Monterrey-Castaño et al. 2010; Martin et al. 2012; Yusef-Zadeh et al. 2013). Here we provide a new tracer of extended neutral gas by identifying radio dark clouds within the molecular ring. The presence of radio dark clouds is consistent with a reservoir of neutral gas that feeds star formation activity close to Sgr A*.

Recent radio images of the Galactic center have revealed a large number of radio dark clouds (Yusef-Zadeh 2012). These features coincide with cool neutral clouds embedded in a hot ionized medium, tracing volumes where there is a deficiency of free-free radio continuum emission. Figures 10(a) and (b) show the distribution of ionized gas surrounding Sgr A* at 7 mm (Yusef-Zadeh et al. 2014). We note three dark features, two near the N and E arms of the mini-spiral, and one near the IRS 13 complex. The darkest features lie to the east of IRS 13E and SE of IRS 13N, identified by a red circle with a diameter $\sim 1''$. We suggest that these dark features are associated with radio dark clouds. Interferometric errors due to incomplete sampling of UV plane also produce dark features. However, the regions labeled in Figure 10 have been detected in radio images

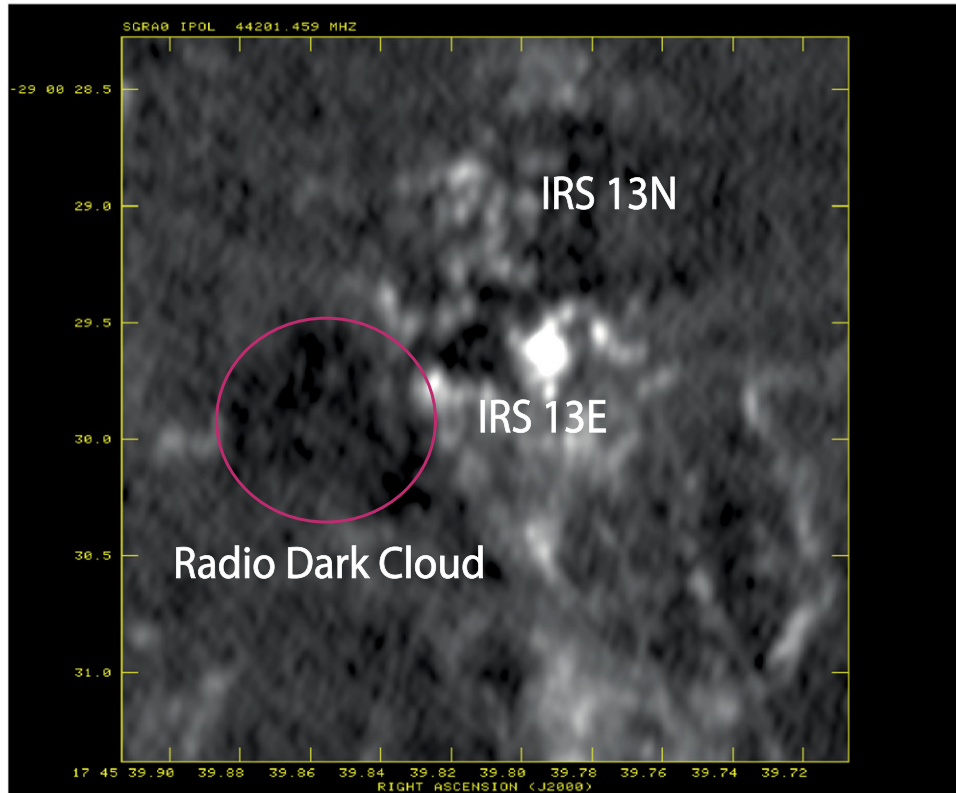
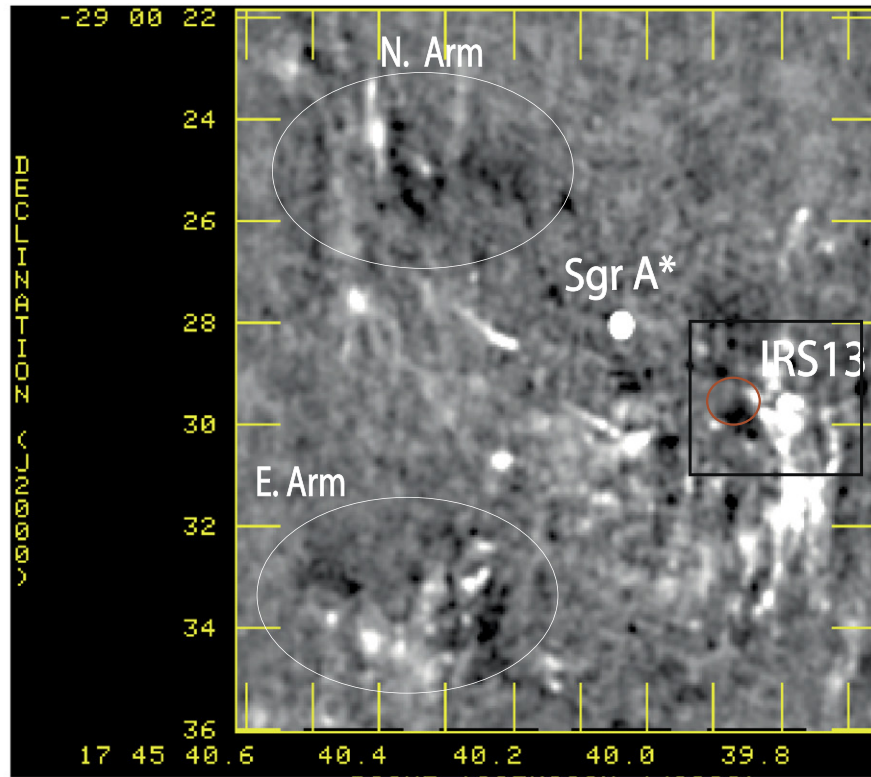


Figure 10. Top: a 44 GHz continuum image with a spatial resolution of $0''.17 \times 0''.15$ ($PA = -0^\circ.35$). Bottom: enlarged view of the region drawn as a black square in the top panel, including both IRS 13E and IRS 13N clusters. The spatial resolution of this image at 7 mm is 82×42 mas ($PA = -5^\circ.5$) (Yusef-Zadeh et al. 2014). The white ellipses in the top panel and the red circle in the bottom one point to radio dark clouds.

at multiple wavelengths based on different observations, suggesting that they are real features. Future high-resolution molecular line observations should confirm our interpretation

of radio dark clouds. The mean flux density averaged over the red circle near IRS 13 is fainter by 0.1–0.2 mJy than the region immediately outside the circled region. The difference between

the flux density of the ambient gas toward and away from the cloud suggests that the depth of the ionized layer is 5–10 times bigger than the dimension of the radio dark cloud. This radio dark cloud may be tracing the molecular material associated with ongoing star formation near IRS 13N. Similarly, the radio dark cloud near the N and E arms indicates that the ionized gas in the mini-spiral feature is well mixed with layers of molecular gas, as traced by dark radio features. In this case, the length of the ionized layer in the N and E arms is two to three times larger than the size of the clouds $\sim 8''$ (~ 0.3 pc) associated with the N and E arms.

4. SUMMARY AND CONCLUSIONS

We have presented five different lines of evidence in favor of ongoing star formation near Sgr A*. First, we reported the detection of 13 water masers with multiple and single velocity components. After their comparison with known OH/IR stars, many of the newly detected water masers are likely to be interstellar tracing star formation activity. The spatial correlation of SiO and HCN (1-0) line emission with water masers provided additional support that star formation activity taking place in the molecular ring. Second, we investigated SED modeling of 64 infrared excess sources in the inner pc of Sgr A*. This study indicated that there are massive YSO candidates in this region. The well-fit YSO models to 19 stellar sources gave us a handle on the total stellar mass ~ 139 and $\sim 119 M_{\odot}$ in Stage I and Stage II, respectively. Using the limited number of YSO candidates, the star formation rate within 1 pc of Sgr A* was estimated to be $\sim 1 \times 10^{-2} M_{\odot} \text{ yr}^{-1}$. We suggested the possibility that the YSO candidates originate in the residual outer regions of the original gas disk within which the central cluster of massive stars was formed. We argued that stellar bow shock sources in this region arise from the interaction of stellar winds from YSO disks with the stream of ionized gas associated with the mini-spiral H II region and/or with the UV radiation field from the central cluster. Third, the presence of several clumps of SiO line emission suggested tracers of ongoing star-forming sites in the molecular ring and in the immediate vicinity of Sgr A*. We identified a bipolar outflow candidate in one of the clumps of SiO emission in the molecular ring. This provided one of the clearest signature of ongoing star formation activity in the ring. Our LVG analysis of SiO lines indicated a typical molecular density $\sim 10^6 \text{ cm}^{-3}$ with an assumed kinetic temperature ~ 150 K. The total mass swept by protostellar outflow that produced a clump of SiO (5-4) emission was estimated to be $\sim 68 M_{\odot}$. Fourth, we presented an EW Ridge of ionized gas with an extent of $20''$ (0.8 pc). The position–velocity diagram of the Ne II line emission along the length of the EW ionized Ridge showed a red and blue velocity component, which is interpreted as a jet arising from a protostar in the molecular ring. Last, we presented imprints of molecular gas in radio continuum images of the Galactic center. The identified molecular clouds represent a reservoir of molecular gas feeding ongoing star formation activity within the inner parsec of Sgr A*.

Future high-resolution observations of this region will provide us with details of massive star formation subject to tidal effects by the nuclear cluster and the massive black hole. Studies of star formation in the Galactic center region where gravitational potential is dominated by Sgr A* provide far reaching understanding of the mode of star formation in the nuclei of more active galaxies hosting true SMBHs.

We are grateful to S. Gillessen and the MPE group for providing us with a $3.8 \mu\text{m}$ image of the Galactic center. This work is partially supported by the grant AST-0807400 from the NSF. The National Radio Astronomy Observatory is a facility of the National Science Foundation, operated under a cooperative agreement by Associated Universities, Inc. We thank the referee for useful comments. This paper makes use of the following ALMA data: ADS/JAO.ALMA#2011.0.00005.SV Project code. ALMA is a partnership of ESO (representing its member states), NSF (USA) and NINS (Japan), together with NRC (Canada) and NSC and ASIAA (Taiwan), in cooperation with the Republic of Chile. The Joint ALMA Observatory is operated by ESO, AUI/NRAO and NAOJ.

REFERENCES

- Amo-Baladron, M. A., Martn-Pintado, J., Morris, M. R., et al. 2009, *ApJ*, **694**, 943
- Beloborodov, A. M., Levin, Y., Eisenhauer, F., et al. 2006, *ApJ*, **648**, 405
- Bonnell, I. A., & Rice, W. K. M. 2008, *Sci*, **321**, 1060
- Buchholz, R. M., Witzel, G., Schödel, R., & Eckart, A. 2013, *A&A*, **557**, 82
- Caswell, J. L., Breen, S. L., & Ellingsen, S. P. 2011, *MNRAS*, **410**, 1283
- Christopher, M. H., Scoville, N. Z., Stolovy, S. R., & Yun, M. S. 2005, *ApJ*, **622**, 346
- Clenet, Y., Rouan, D., Gendron, E., et al. 2004, *A&A*, **417**, L15
- Draine, B. T., & Lee, H. M. 1984, *ApJ*, **285**, 89
- Eckart, A., Muzic, K., Yazici, S., et al. 2013, *A&A*, **551**, 18
- Etxaluze, M., Smith, H. A., Tolls, V., et al. 2006, *AJ*, **142**, 134
- Gatley, I., Jones, T. J., Hyland, A. R., Wade, R., et al. 1986, *MNRAS*, **222**, 299
- Genzel, R., Eisenhauer, F., & Gillessen, S. 2010, *RvMP*, **82**, 3121
- Gibb, A. G., Davis, C. J., & Moore, T. J. T. 2007, *MNRAS*, **382**, 1212
- Gibb, A. G., Richer, J. S., Chandler, C. J., & Davis, C. J. 2004, *ApJ*, **603**, 198
- Goicoechea, J. R., Etxaluze, M., Cernicharo, J., et al. 2013, *ApJL*, **769**, L13
- Habing, H. J. 1996, *A&ARv*, **7**, 97
- Irons, W. T., Lacy, J. H., & Richter, M. J. 2012, *ApJ*, **755**, 90
- Jackson, J. M., Geis, N., Genzel, R., et al. 1993, *ApJ*, **402**, 173
- Jalali, B., Pelupessy, F. I., Eckart, A., et al. 2014, *MNRAS*, **444**, 1205
- Koepferl, C. M., Robitaille, T. P., Morales, E. F. E., & Johnston, K. G. 2015, *ApJ*, **799**, 53
- Kroupa, P. 2001, *MNRAS*, **322**, 231
- Lacy, J. H., Richter, M. J., Greathouse, T. K., et al. 2002, *PASP*, **114**, 153
- Lindqvist, M., Habing, H. J., & Winnberg, A. 1992, *A&A*, **259**, 118
- Li, J., An, T., Shin, Z.-Q., & Miyazaki, A. 2010, *ApJ*, **720**, 56
- Levine, D. A., Figer, D. F., Morris, M., & McLean, I. S. 1995, *ApJ*, **447**, 101
- Lu, J. R., Ghez, A. M., Hornstein, S. D., et al. 2009, *ApJ*, **690**, 1463
- Mapelli, M., Gualandris, A., & Hayfield, T. 2013, *MNRAS*, **436**, 3809
- Mapelli, M., Hayfield, T., Mayer, L., & Waddle, J. 2012, *ApJ*, **749**, 168
- Martin, S., Martin-Pintado, J., Montero-Castaño, M., Ho, P. T. P., & Blundell, R. 2012, *A&A*, **539**, 29
- Mills, E. A. C., Gusten, R., Requena-Torres, M. A., et al. 2013, *ApJ*, **779**, 47
- Montero-Castaño, M., Hernstein, R. M., & Ho, P. T. P. 2009, *ApJ*, **695**, 1477
- Moulata, J., Eckart, A., Viehmann, T., et al. 2004, *A&A*, **425**, 529
- Muzic, K., Eckart, A., Schödel, R., et al. 2010, *A&A*, **521**, 13
- Nayakshin, S., Cuadre, J., & Springel, V. 2007, *MNRAS*, **379**, 21
- Nishiyama, S., & Schödel, R. 2013, *A&A*, **549**, 16
- Paumard, T., Genzel, R., Martins, F., et al. 2006, *ApJ*, **643**, 1011
- Preger, M., Moulata, J., Eckart, A., et al. 2008, *A&A*, **478**, 127
- Poglitsch, A., Waelkens, C., Geis, N., et al. 2010, *A&A*, **518**, L2
- Povich, M. S., Townsley, L. K., Broos, P. S., et al. 2011, *ApJS*, **194**, 6
- Requena-Torres, M. A., Gusten, R., Weib, A., et al. 2012, *A&A*, **542**, 21
- Robitaille, T. P., Whitney, B. A., Indebetouw, R., et al. 2006, *ApJS*, **167**, 256
- Robitaille, T. P., Whitney, B. A., Indebetouw, R., & Wood, K. 2007, *ApJS*, **169**, 328
- Sanchez-Bermudez, J., Schödel, R., Alberdi, A., et al. 2014, *A&A*, **567**, AA21
- Schödel, R., Najarro, F., Muzi, K., & Eckart, A. 2010, *A&A*, **511**, 18
- Sjouwerman, L. O., Lindqvist, M., van Langevelde, H. J., & Diamond, P. J. 2002, *A&A*, **391**, 967
- Sjouwerman, L. O., & van Langevelde, H. J. 1996, *ApJL*, **461**, L41
- Smith, I. L., & Wardle, M. 2014, *MNRAS*, **437**, 3159
- Tanner, A., Ghez, A. M., Morris, M., et al. 2002, *ApJ*, **575**, 860
- Tanner, A., Ghez, A. M., Morris, M. R., & Christou, J. C. 2005, *ApJ*, **624**, 742
- Viehmann, T., Eckart, A., Schödel, R., et al. 2005, *A&A*, **433**, 117
- Viehmann, T., Eckart, A., Schödel, R., et al. 2006, *ApJ*, **642**, 861

- Wallerstein, G., & Knapp, G. R. 1998, [ARA&A](#), **36**, 369
- Wardle, M., & Yusef-Zadeh, F. 2008, [ApJL](#), **683**, L37
- Wardle, M., & Yusef-Zadeh, F. 2012, [ApJL](#), **750**, L38
- Wardle, M., & Yusef-Zadeh, F. 2014, [ApJL](#), **787**, L14
- Whitney, B. A., Sewilo, M., Indebetouw, R., et al. 2008, [AJ](#), **136**, 18
- Whitney, B. A., Wood, K., Bjorkman, J. E., & Wolff, M. J. 2003, [ApJ](#), **591**, 1049
- Yoshikawa, T., Nishiyama, S., Tamura, M., et al. 2013, [ApJ](#), **778**, 92
- Yusef-Zadeh, F. 2012, [ApJL](#), **759**, L11
- Yusef-Zadeh, F., Braatz, J., Wardle, M., & Roberts, D. 2008, [ApJL](#), **683**, L147
- Yusef-Zadeh, F., Hewitt, J. W., Arendt, R. G., et al. 2009, [ApJ](#), **702**, 178
- Yusef-Zadeh, F., Lacy, J. H., Wardle, M., et al. 2010, [ApJ](#), **725**, 1429
- Yusef-Zadeh, F., Roberts, D. A., Bushouse, H. A., et al. 2014, [ApJ](#), **792**, 1
- Yusef-Zadeh, F., Royster, M., Wardle, M., et al. 2013, [ApJL](#), **767**, L32
- Yusef-Zadeh, F., Stolovy, S. R., Burton, M., et al. 2001, [ApJ](#), **560**, 749
- Yusef-Zadeh, F., & Wardle, M. 1993, [ApJ](#), **405**, 584
- Zhao, J.-H., Blundell, R., Moran, J. M., et al. 2010, [ApJ](#), **723**, 1097